Structure, electric and thermoelectric properties of binary ZnO-based ceramics doped with Fe and Co

A.V. Pashkevich[a,b], A.K. Fedotov[a], E.N. Poddenezhny[c], L.A. Bliznyuk[d], J.A. Fedotova[a], N.A. Basov[d], A.A. Kharchanka[a], P. Zukowski[e], T.N. Koltunowicz[e,*], O.V. Korolik[b], V.V. Fedotova[d]

[a] Research Scientific Institute for Nuclear Problems of Belarusian State University, 11, Bobruiskaya Str., 220030 Minsk, Belarus
[b] Belarusian State University, 4, Nezavisimosti Av, 220030 Minsk, Belarus
[c] P.O. Sukhoi Gomel State Technical University, 48, Oktyabrskya Av., 246746 Gomel, Belarus
[d] National Practical Center of National Academy of Science for Material Science, 19, P. Brovka Str., 220072 Minsk, Belarus
[e] Lublin University of Technology, 38d, Nadbystrzycka St, 20–618 Lublin, Poland

ARTICLE INFO

ABSTRACT

We have studied the interconnection between structure (grain sizes, chemical and phase composition, porosity) and some electric properties (resistivity, Hall and Seebeck coefficients, as well as power factor, concentration and mobilities of carriers) in composite ceramics $(ZnO)_z[(TM)_xO_y]_{1-z}$ (TM = Fe and Co – transition metals, $0 \leq x \leq 3$; $1 \leq y \leq 4$, $0.5 \leq z \leq 10$ wt%), prepared by one-step and/or two-step annealing on air of powder mixtures of ZnO and TM oxides. The structure of ceramic samples was studied by X-ray diffraction (XRD), Mossbauer (MS) and Raman (RS) spectroscopies, scanning electron microscopy (SEM), energy-dispersive X-ray (EDX) analysis and magnetometry. It was proved that phase composition of $(ZnO)_z[(TM)_xO_y]_{1-z}$ ceramics depends on the type of doping agents. Addition of CoO to ZnO results in the formation of solid solutions with wurtzite structure after two-step annealing independently on Co concentration $z \leq 10$ wt%. Addition of Fe_xO_y to ZnO results in the formation of the samples with three phase components after synthesis: submicron grains of wurtzute-like structure with large grains of $ZnFe_2O_4$ ferrite with spinel structure and residual oxides Fe_xO_y used as dopant in powder mixture. SEM measurements evidence that size of the wurtzite phase grains decreases from several tens of micrometers when using the one-step synthesis to a submicron level for the case of the two-step technology. Temperature dependences of electrical resistivity $\rho(T)$, as well as Hall and Seebeck coefficients in the undoped ZnO in th range of 6–500 K have shown a competition of the Mott and Shklovsky-Efros variable range hopping conductance (due to disordering), percolative one (due to formation of large-scaled potential relief) and a standard electron transport by C−band. It was found that C−band contribution to the carrier transport in ceramic samples $(ZnO)_z[(TM)_xO_y]_{1-z}$ above 100 K was provided by both low and deep donor centers which have been formed in the wurtzite phase $Zn_{1-\delta}(TM)_\delta O$. For example, in the TM doped samples we observed intrinsic shallow levels with ionization energies of about $\Delta E_1 = (0.04–0.05)$ eV as well as extrinsic deep levels with $\Delta E_2 = (0.24–0.37)$ eV. The iron doping of ZnO-based ceramic samples increased the room temperature Seebeck coefficient $S(300$ K) in average. In so doing, the $S(300$ K) dependence on electron concentration n of the studied samples $(ZnO)_z(Fe_xO_y)_{1-z}$ approached maximal values (up to 1000 μV/K) at $n = 10^{21}$ m^{-3}. At the same time ZnO doping with Co resulted in more weak increase (up to 1.3–1.5 times) of $S(300$ K) values. Practically threefold growth of $S(300$ K) doe to Fe doping was attributed by us to the influence of particles of ferrite) formed in wurtzite matrix. The power factor $P = (S^2/\rho)$, estimated for the studied samples, evidenced that for both dopants it's the highest values (= 10^{-5} W/K·m) were approached in the $(ZnO)_z[(TM)_xO_y]_{1-z}$ ceramics with the lowest resistivity values.

* Corresponding author.
E-mail address: t.koltunowicz@pollub.pl (T.N. Koltunowicz).

1. Introduction

Zinc oxide, possessing a unique combination of physical properties and a variety of forms, has remained the object of strong attention of many researchers for several decades. Functional materials based on ZnO in the form of ceramics are increasingly used in optoelectronics, sensors, and converters of various types of energy into electrical energy [1,2]. Currently, special attention is paid to the search for ZnO-based ceramic materials doped with different impurities, in particular, with transition metals (TMs), which results in improving of their properties. This invokes an enhanced search for correlations between structure (grain sizes, phase and chemical compositions, porosity, etc.) and electronic properties of composite ceramics, as well as striving of their cost-effective production technologies [3–7]. Such ceramics have a number of advantages compared with polycrystalline ingots and thin films, as well as single crystals obtained using more expensive technologies. Ceramic technologies make it possible to manufacture products of various shapes and sizes changing their morphology, structural and phase state. This allows to control effectively their functional properties by changing sintering temperatures, duration and atmosphere of synthesis and the following heat treatments, as well as the type of doping agents in powder mixtures [4–6,8–10].

There are yet one important application of ZnO-based ceramics that attracts increasing attention last years. They are the most hopeful n-type thermoelectric materials, also possessing low toxicity, high electron mobility, thermal stability, and corrosion resistance. However, the thermal conductivity κ of pure ZnO is so high that the values ZT = $S^2\sigma T/\kappa$ (Z is the figure-of-merit, T is the absolute temperature, S is the Seebeck coefficient, and σ is the electrical conductivity) becomes lower than is required for practical uses. Therefore, in context of thermoelectrical applications, it is important to suppress this high κ without sacrificing the S and σ values. So, the doping is one of the main instruments for matching of κ, S and σ values to increase ZT.

ZnO-based oxide system has a rich variety of doping choices for altering the microstructure as well as tuning thermoelectric and transport properties. As was mentioned in [11–17], examples of dopant elements, which influence the thermoelectric and transport properties, are Al, Bi, Co, Fe, Ni, Ga, Mn, Sb, Sn and even their dual compositions. The mentioned papers provide some useful information on the doping effect and correlation between structure and properties, while it lacks a systematic investigation of the thermoelectric properties, especially with combined observation on the microstructure.

Since literary sources also indicate that oxides of transition elements, as well as some of their combinations with ZnO, have high values of the Seebeck effect and low thermal conductivity [8,12,18–23], it can be expected that preparation of ZnO-based ceramic compositions with their participation will also lead to an improvement in thermoelectric properties. On the other side, we should note that thermoelectric and transport properties of the Fe- and Co doped ZnO ceramics are not yet deeply explored. Light doping of Fe into ZnO was found not to cause any changes in microstructure. Nevertheless, there were a few works on Fe highly doped ZnO reporting the formation of oxide defect structure including inversion domain structures [22] or antiphase modulated layers [21], both of which are in the length scale of 10 nm. However, few systematic efforts have been made to explore the thermoelectric properties of Fe- and Co-doped ZnO; neither the thermal conductivity nor the electrical conductivity and the Seebeck coefficient have been investigated. It is of primary interest in the present work to look into the effect of phase equilibria and microstructure on thermoelectric and transport properties of Fe- and Co-doped ZnO ceramics.

Binary compositions $(ZnO)_z[(TM)_xO_y]_{1-z}$, where TM = Fe, Co, are of additional research interest [4–6,24–43] because their structural, electrical, magnetic and optical properties depend not only on the concentration of TM impurities, but also whether they are evenly distributed, being incorporated into the crystal lattice of wurtzite matrix, or form submicronic/nanosized grains and magnetic clusters of different nature. Such hybrid nanocomposite materials containing magnetic particles with high spin polarization (for example, $(TM)_xO_y$/ZnO, $ZnFe_2O_4$/ZnO, etc.) can be used in spintronic devices [39–52], microwave absorption [53], photocatalysts [54], cancer immunotherapy [55], for detoxification of water [56], for gas-sensitive adsorption sensors based on zinc ferrite [57] and in other applications as well.

Studies of the doping effect on single crystals, polycrystalline films, as well as nanostructured powders, tetrapods and nanowires are widely known from the literature [58–64]. At the same time, the studies of ZnO-based compositions sintered by ceramic technologies are far from completion (probably, with the exception of varistor ceramics [3,4], where d-TMs are often incorporated into ZnO matrix during the synthesis process). In particular, we are far from understanding of such influences as incorporation of magnetic oxides in ZnO and changes in the synthesis/annealing regimes on the structure and magnetic state of the resulting phases, as well as on carrier transport, Seebeck and Hall effects and other properties [4,5,39,58,60–63]. Modeling and experimental studies show that in an ideal wurtzite-like ZnO-based samples with TM ions both a relatively shallow and more deep donor centers with an ionization energies of 0.1–0.4 eV are observed [63,65,66].

In this connection, the paper is mainly focused on the study of the impact of the synthesis/annealing regimes as well as type of doping agents (Fe_xO_y or CoO) on interconnection between phase structure, chemical composition and dopants distribution, grain sizes and porosity, on one side, and electric and thermoelectric properties of binary $(ZnO)_z[(TM)_xO_y]_{1-z}$ ceramics, on other side.

2. The subject of study and diagnostic methods

The initial homogeneous powder mixtures were prepared in stainless steel grinder with hard-alloy balls in the presence of alcohol as humidifier. The dispersion of particle sizes in the initial powder mixtures was about 10–50 µm after 12 h grinding. In order to remove moisture at the preparation of samples, we dried the initial powder mixtures at 500–900 °C until a constant weight approached. After mixing-up of the dried powders, we added 3 wt% of special organic glue and subjected the powder mixtures to uniaxial pressing at 200 MPa to form tablets with diameter of 10–18 mm and thickness of 2–5 mm.

For preparation of $(ZnO)_z[(TM)_xO_y]_{1-z}$ tablets, we used either two-step (samples 6–15) or one-step (samples 1–5, 15–21) technologies. Two-step technology included pre-sintering procedure (1st step) and subsequent annealing (2nd step). After pre-sintering of ceramic tablets on the 1st stage, they were grinded again into powder of submicronic sizes, mixed with the glue and again compacted at 200 MPa. After subjection of compacted tablets to the final annealing on air at 1100–1200 °C for 2–3 h (see, Table 1), they were cooled with the furnace at a speed of 200–300 °C/h both after every pre-sintering procedure and annealing process. Note that the sample 9 in Table 1 prepared from powder mixture ($FeO + Fe_2O_3$) had another pre-sintering/annealing mode. Make yet one remark concerning initial ZnO powder used in our experiments. As far as we used ZnO powders from two different producers for the preparation of Fe- and Co-doped ceramic samples, measurements of electric properties for pure (undoped) ZnO ceramic samples have displayed slightly different values (see, below). In Table 1 these samples were labeled as ZnO-A (when using of Fe-doping) and ZnO-B (when using of Co-doping).

Table 1

Compositions and preparation regimes for the studied ZnO and $(ZnO)_z[(TM)_xO_y]_{1-z}$ samples produced by the one- and/or two-step ceramic technologies.

№	Sample designations and labeling	Pre-sintering temperature, °C	Time of pre-sintering temperature, h	Final annealing temperature, °C	Time of final annealing, h
1	ZnO-A	1100	2	–	–
2	ZnO-B	900	2	–	–
3	$(ZnO)_{98}(FeO)_2$-1	900	2	–	–
4	$(ZnO)_{95}(FeO)_5$-1	900	2	–	–
5	$(ZnO)_{90}(FeO)_{10}$-1	900	2	–	–
6	$(ZnO)_{98}(Fe_2O_3)_2$-1	900	2	–	–
7	$(ZnO)_{95}(Fe_2O_3)_5$-1	900	2	–	–
8	$(ZnO)_{90}(Fe_2O_3)_{10}$-1	900	2	–	–
9	$(ZnO)_{98}(Fe_3O_4)_2$-1	900	2	–	–
10	$(ZnO)_{95}(Fe_3O_4)_5$-1	900	2	–	–
11	$(ZnO)_{90}(Fe_3O_4)_{10}$-1	900	2	–	–
12	$(ZnO)_{90}(FeO)_{10}$-2	900	2	1200	2
13	$(ZnO)_{90}(Fe_2O_3)_{10}$-2	900	2	1200	2
14	$(ZnO)_{90}(Fe_3O_4)_{10}$-2	900	2	1200	2
15	$(ZnO)_{90}(FeO+Fe_2O_3)_{10}$-2	900	4	1200	48
16	$(ZnO)_{98}(CoO)_2$-1	1100	3	–	–
17	$(ZnO)_{95}(CoO)_5$-1	1100	3	–	–
18	$(ZnO)_{90}(CoO)_{10}$-1	1100	3	–	–
19	$(ZnO)_{90}(CoO)_{10}$-2	900	2	1200	2
20	$(ZnO)_{95.0}(CoO)_{5.0}$-1	1100	3	–	–
21	$(ZnO)_{99.5}[(CoO)_{5.0}·(ZnO)_{95.0}]_{0.5}$-1	1100	3	–	–

* Numbers 1 and 2 in the samples labeling after chemical formula in the second column denote one- or two-step synthesis technologies, respectively

** TM – transition metals (Fe or Co)

To prepare ZnO and $(ZnO)_z[(TM)_xO_y]_{1-z}$ samples, we used standard ceramic technology of sintering on air [4,41]. High purity powders of ZnO, FeO, α-Fe_2O_3, Fe_3O_4 and CoO or their mixtures were used as the starting components for the samples preparation before their heat treatment. When calculating the weights of band-and-hook hinges, we used the formula $(ZnO)_z[(TM)_xO_y]_{1-z}$, where full mass z of TM oxide powders z in the initial powder mixtures changed between 0.5 and 10.0 wt%.

Structural characterization of ceramic samples was carried out at room temperature by X-ray diffraction analysis (XRD), which was performed on an automated devices DRON-3 M and DRON-4 (Russia). We used Cu-K_α radiation and the scanning steps by 2θ angles about 0.03 degrees in the range 20–60 degrees. The exposure time was about five seconds in every point. X-ray patterns were fitted using the FullProf code based on the Rietveld method [67].

Raman spectroscopy (RS) for the structural characterization of ceramic samples was performed on a Nanofinder High-End confocal spectrometer (LOTIS TII, Belarus-Japan). To excite the signal, we used a solid-state laser with wavelength 532 nm and power 20 mW. The laser beam was focused on the surface of the sample with an objective 50x (numerical aperture of 0.8). Laser spot at room temperature was about 200×200 nm, that allowed to analyze the structure of single grains and phase inclusions. The power of incident laser radiation was attenuated to 2 mW in order to avoid thermal damage of the sample surface. The backscattered light was dispersed by a 600 mm^{-1} diffraction grating, which made it possible to obtain a spectral resolution no worse than 3 cm^{-1}. Spectral calibration was carried out by lines of a gas-discharge lamp, which ensured accuracy no worse than 3 cm^{-1}. A cooled silicon CCD matrix was used as a photodetector. The signal accumulation time was 30 s

To estimate shape and sizes of grains, we used the scanning electron microscopy (SEM) in the mode of secondary electrons. SEM images were done on the devices LEO 1455VP Oxford Instruments (Great Britain) and Tescan Vega 3LMU (Czech Republic). These devices were supplied with the energy-dispersive X-ray (EDX) analysis attachments to measure concentrations of chemical elements.

To detect the porosity of the samples studied, we used the microscope Olimpus GX41 (Japan) supplied with the software AutoScan 005.

To detect magnetic status and local atomic order as well as charge state of Fe ions and iron oxides content in the studied samples, we used Mössbauer spectroscopy (MS). MS was carried out in temperature range of 20–300 K using an MS4 (SEE Co) Mössbauer spectrometer (USA) for powder samples in a transmission geometry with a ^{57}Co/Rh source (20 μCi). Mössbauer spectra were fitted by the Rankur method using the MOSMOD code [68]. The values of isomer shifts *IS* are given with respect to α-Fe phase at room temperature.

The magnetic properties (magnetization curves, coercivity, etc.) of composite ceramics doped with iron were studied on Vibrating Sample Magnetometer (VSM) Quantum Design VSM-PPMS (USA) in the range of temperature $T = 5$–300 K and the applied magnetic fields $B = 0$–9 T.

The temperature and magnetic field dependences of resistivity $\rho(T, B)$ and the Hall constant $R_H(T, B)$ in the studied ceramics were measured on the rectangular samples with a width of 2–3 mm and a length of 7–10 mm, cut from the described above synthesized tablets. We used silver current contacts, which were prepared at the two butts of the samples, and also two potential and two Hall contacts, which were prepared between current contacts at the wide edge of every sample. In this measurements we used the High Field Measurement System (HFMS) supplied with a closed-cycle refrigerator (Cryogenic Ltd., London). The sample to be measured was mounted in a special platform on the probe containing magnet field sensor, thermometers, heaters and special heated shields. The probe with the mounted sample was placed inside the channel of superconducting solenoid in the cryostat of the HFMS and connected to an automated measuring system.

The dependences of $\rho(T, B)$ and $R_H(T, B)$ ware measured in the temperature range of 6–300 K and in magnetic fields with magnetic induction $0 \leq B \leq 8$ T. The current through the sample was set and measured by the Sub-Femtoamp Remote SourceMeter Keithley 6430 (USA), which made it possible to measure the electrical resistance of the samples in the range of 100 μΩ –10 GΩ with an accuracy not worse than 0.1%. The temperature of the samples was controlled by LakeShore thermodiodes calibrated with an accuracy of 0.0005 K and having a reproducibility of 0.001 K, which allowed to stabilize and measure the temperature with the LakeShore 331 controller (USA). The accuracy of measuring the resistivity and the Hall constant was not worse than 5%, which was determined mainly by the inaccuracy of measurement of the samples geometric dimensions, the width of potential electrical contacts and distances between them.
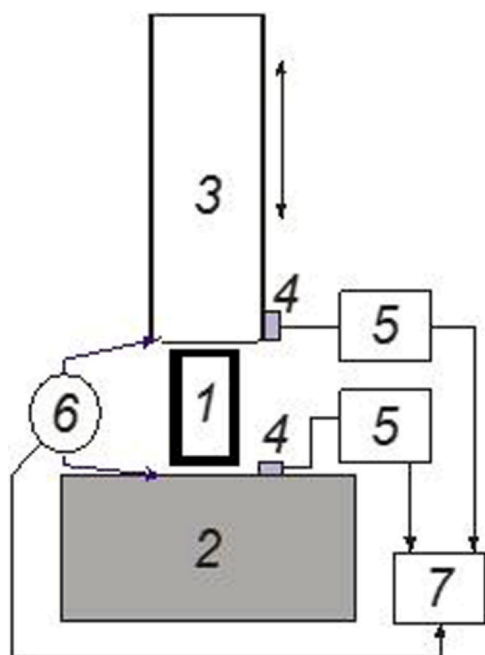
Fig. 1. Schematic illustration of a setup for measuring thermopower and resistivity at room temperature: *1* – test sample; *2* – a copper plate; *3* – a movable copper plate with a heater; *4* – resistance thermometers; *5* – source multimeter Agilent 34410 A; *6* – voltmeter Agilent 34411 A; *7* – managing personal computer.

Measurement of thermoEMF S_{300} and electrical resistivity ρ_{300} at room temperature (300 K) was carried out using the handmade setup shown in Fig. 1. To measure the Seebeck coefficient and resistivity, the described above samples 1 were clamped between copper plates 2 and 3 (movable and with heater) and thermometers 4. To supply the uniform distribution of current and temperature at the contacts between sample 1 and copper plates 2 and 3, an indium layer was deposited by ultrasonic brazing on the ends of the samples. After the temperature values on the sample became stationary, the thermopower and voltage drop values were recorded by source multimeter 5 and voltmeter 6.

Seebeck coefficient S_{300} was calculated by the formula.

$$S_{300} = U_{av}/\Delta T, \tag{1}$$

where $\Delta T = (T_1 - T_2)$, T_1 and T_2 are the temperatures of hot (3) and cold (2) copper plates, and U_{av} is the thermopower indication for several (at least three) repeated measurements. The accuracy of determining the Seebeck coefficient and electrical resistivity was about 10%.

3. Structure and phase composition of the studied ceramic samples

Table 2 shows the main structural characteristics of phases formed in ceramic tablets, prepared by one- or two-step technologies by regimes presented in Table 1. Among them are porosity, the lattice parameters (*a* and *c*) of wurtzite phase $Zn_{1-\delta}(TM)_\delta O$ and cubic ferrite $ZnFe_2O_4$ phase, as well as the average concentrations of TM in the tablets and concentration δ of TM in the wurtzite phase $Zn_{1-\delta}(TM)_\delta O$ detected by EDX method.

Let us note the main structural features of $(ZnO)_z[(TM)_xO_y]_{1-z}$ tablets studied by SEM and EDX methods. Examples of SEM images for one-stage tablets $(ZnO)_{90}(FeO)_{10}$-1 (sample 3) and $(ZnO)_{90}(CoO)_{10}$ (sample 18) with similar weight content of doping agents are shown in Fig. 2(a and d). It can be seen that in ceramics $(ZnO)_{90}(CoO)_{10}$ (Fig. 2a) the size of the wurtzite phase granules was within 1–2 µm, while the size of wurtzite grains in the $(ZnO)_{90}(FeO)_{10}$-1 tablets (Fig. 2b) was significantly higher (– 1–10 µm). In addition, in $(ZnO)_{90}(FeO)_{10}$-1 ceramics, a small number of granules with sizes up to 20–40 µm were observed (Fig. 2d). As shown by EDXR studies, these large granules were enriched with iron in these ceramic samples (Fig. 2e). At the same time, for ceramic composites $(ZnO)_{90}(CoO)_{10}$, the images of the distribution of cobalt and zinc in (Fig. 2b and c) by EDXR measurements indicate the complete solubility of Co in ZnO with the absence of granules with an increased cobalt content.

Note one more important feature of the grain structure of ceramic pellets $(Fe_xO_y)_{10}(ZnO)_{90}$, which follows from Figs. 3 and 4. As was shown by SEM studies earlier [69], after preliminary sintering on the 1st stage, the sizes of wurtzite granules in ceramic tablets $(Fe_xO_y)_{10}(ZnO)_{90}$ varied, as a rule, from 1 to 10 micrometers (see Fig. 3a–c). The sizes of granules in ceramics obtained by a one-stage technology (at lower sintering temperatures) were set mainly by the grain sizes in the initial powders. After relatively short high-temperature annealing at the second stage of tablets preparation, the size of the most grains sharply decreased to 500–800 nm.

Table 2

Porosity of tablets, as well as TM content δ and lattice parameters (*a* and *c*) in the studied phases $Zn_{1-\delta}(TM)_\delta O$ and $(ZnO)_z[(TM)_xO_y]_{1-z}$.

№	Sample	Porosity, %	Mean TM content, at%	Concentration of TM (δ) in $Zn_{1-\delta}(TM)_\delta O$,at%	Lattice parameters of $Zn_{1-\delta}(TM)_\delta O$, nm	Lattice parameter of $Zn(TM)_2O_4$,nm
1	ZnO-A	14.6	0	0	*a* = 0.32472 *c* = 0.51965	–
2	ZnO-B	12.3	0	0	*a* = 0.32509 *c* = 0.52023	–
3	$(ZnO)_{98}(FeO)_2$-1	14.2	–	–	*a* = 0.32429 *c* = 0.51844	–
4	$(ZnO)_{95}(FeO)_5$-1	12.3	–	–	*a* = 0.32462 *c* = 0.51939	0.84271
5	$(ZnO)_{90}(FeO)_{10}$-1	17.5	1.2	0.77	*a* = 0.32548 *c* = 0.52105	0.84292
6	$(ZnO)_{98}(Fe_2O_3)_2$-1	15.0	–	–	*a* = 0.324856 *c* = 0.520019	0.83457
7	$(ZnO)_{95}(Fe_2O_3)_5$-1	15.8	–	–	*a* = 0.324698 *c* = 0.520019	0.84298
8	$(ZnO)_{90}(Fe_2O_3)_{10}$-1	16.0	2.3	0.82	*a* = 0.324706 *c* = 0.519645	0.84289
9	$(ZnO)_{98}(Fe_3O_4)_2$-1	14.8	–	–	*a* = 0.324619 *c* = 0.519934	–
10	$(ZnO)_{95}(Fe_3O_4)_5$-1	15.8	–	–	*a* = 0.32442 *c* = 0.51953	0.84018
11	$(ZnO)_{90}(Fe_3O_4)_{10}$-1	–	2.87	0.69	*a* = 0.32508 *c* = 0.520301	0.84362
12	$(ZnO)_{90}(FeO)_{10}$-2	–	1.01	0.81	*a* = 3.24748 *c* = 5.19836	0.84319
13	$(ZnO)_{90}(Fe_2O_3)_{10}$-2	–	2.81	0.66	*a* = 0.32474 *c* = 0.51980	8.43348
14	$(ZnO)_{90}(Fe_3O_4)_{10}$-2	–	2.98	0.79	a = 0.32474 c = 0.51996	0.84333
15	$(ZnO)_{90}(FeO+Fe_2O_3)_{10}$-2	–	5.04	0,87	a = 0.32501 c = 0.520104	8.43928
16	$ZnO)_{98}(CoO)_2$-1	15.8	0.65	1.15	a = 0.32483 c = 0.51969	no
17	$ZnO)_{95}(CoO)_5$-1	15.2	0.81	2.21	a = 3.24741 c = 5.19522	no
18	$ZnO)_{90}(CoO)_{10}$-1	13.5	2.35	3.25	a = 0.32480 c = 0.51941	no
19	$ZnO)_{90}(CoO)_{10}$-2	–	2.30	3.80	a = 0.324943 c = 0.51974	no
20	$(ZnO)_{95.0}(CoO)_{5.0}$-1	17.5	–	–	a = 0.32512 c = 0.52037	no
21	$(ZnO)_{99.5}[(CoO)_{5.0} \cdot (ZnO_{95.0})]_{0.5}$-1	15.5	–	–	*a* = 0.32512 c = 0.52037	no

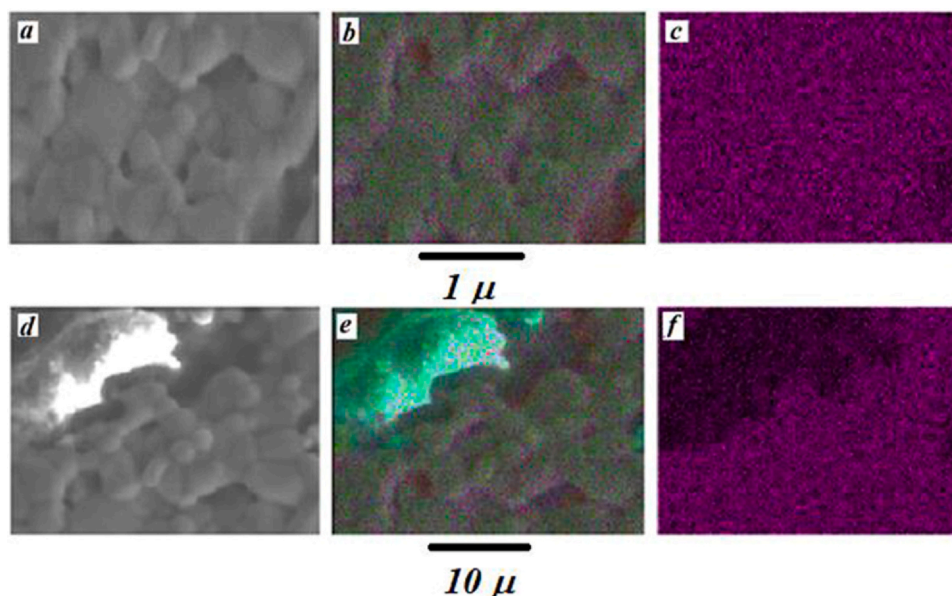**Fig. 2.** Examples of SEM (*a, d*) and EDX (*b, c, e, f*) images in composite ceramics $(ZnO)_{90}(CoO)_{10}$ (sample 12, *a–c*) and $(ZnO)_{90}(FeO)_{10}$ (sample 3, *d–f*): distributions of Co (*b*), Fe (*e*) and Zn (*c, f*).

Nevertheless, as seen in (Fig. 3d–f), some part of granules (relatively low) had dimensions of the order of tens of micrometers and was enriched with iron. The mentioned above decrease of grain sizes after the 2nd (high-temperature) stage of synthesis occurs, in our opinion, due to specificity of their preparation procedure. As noted in Part 2 of this article, the powders, from which the tablets were made in the second stage of synthesis, were obtained by prolonged grinding of the tablets obtained in the first stage. Since the granules of these powders were significantly smaller, the concentration (surface) of grain boundaries in such powders after pressing was significantly higher than in the initial powders. This led to the formation of a higher concentration of recrystallization centers during high-temperature annealing at the second stage of the synthesis, which led to the formation of smaller grains during diffusion at relatively short times of high-temperature annealing.

The example of the SEM image and EDX pattern with iron and zinc distributions in $(Fe_xO_y)_{10}(ZnO)_{90}$ tablets, shown in Fig. 4, confirm the presence of secondary iron-enriched phases containing up to 1–5 at% of iron after 2nd stage annealing. Note also, that, as follows from Table 2, in wurtzite-like $Zn_{1-\delta}(TM)_\delta O$ solid solutions, Fe or Co contents give their values $\delta < 1$ at% for Fe whereas for Co this value approaches about (3.2–3.8) at%.

SEM images of the structure (Fig. 5) and EDX measurements of Co and Zn distribution (Fig. 2b and c) in $(ZnO)_{90}(CoO)_{10}$ pellets confirmed the homogeneity of their structure and the absence of cobalt-enriched regions both after one-step and two-step synthesis.

As follows from our previous X-Ray diffraction measurements [69,70] as well as Fig. 6 and Table 2, the refined XRD data show that lattice parameters *a* and *c* in the wurtzite phase of $Zn_{1-\delta}(TM)_\delta O$ become average less when doping, although the ratio *a/c* stays equal to = 1.60 for all the studied tablets. Underline also, that differently from $(ZnO)_z(Fe_xO_y)_{1-z}$ ceramic pellets, in the samples $(ZnO)_z(CoO)_{1-z}$ we did not observe any extra lines in diffraction patterns for all the studied values of *z* (between 0.5 and 10 wt%), see, Fig. 6 and Table 2. This confirms the lack of ferritic or residual CoO phases in these samples, as was mentioned above.

The micro-Raman spectra for the $(ZnO)_z[(TM)_xO_y]_{1-z}$ pellets were measured intentionally in several local points of the studied ceramic samples, to get either only in the region of the wurtzite phase $Zn_{1-\delta}(TM)_\delta O$ existence or in the grains of the secondary phases (when they were present). Examples of Raman spectra for regions without and with iron-enriched grains are shown in Fig. 7 and Fig. 8, accordingly.

Comparison of lines positions in Raman spectra with ones in literature [64,71,72] confirms the presence of $Zn_{1-\delta}(TM)_\delta O$ wurtzite phase in Fig. 7 and two cubic phases in Fig. 8, which were identified above from RDA spectra as $ZnFe_2O_4$ zinc ferrite and/or residues of the Fe_xO_y doping agents.

Actually, all the spectra in Fig. 7 show a sharp and strong peak at around 435 cm^{-1}, which were assigned to "E2 high mode", that is attributed to ZnO wurtzite in [73]. We also observed the acoustic combinations of A1 and E2 components around 1100 cm^{-1}. The peak at –573 cm^{-1} is referred to be "A1(LO)/E1(LO) phonon mode" and is usually represented to the defect complexes of zinc interstitials and/or oxygen vacancies in ZnO lattice that are enhanced at dopant incorporation [61]. This means that Fe- or Co-doping of ZnO results in the enhancement of the oxygen vacancies content. The broad peak in (Fig. 7b and c) observed at around 665 cm^{-1} are usually ascribed to incorporation of TM-ions into ZnO wurtzite matrix [74]. At the same time, we should note that some of papers interpret this fact as a consequence of activation of vibrating complex connected with intrinsic lattice defects [73].

All the spectra in Fig. 8 were recorded only for regions enriched by iron due to lack of $ZnCo_2O_4$ phase in the studied Co-doped ZnO ceramic samples. They indicate the high frequency "first order mode A1g" between 1000 and 1400 cm^{-1}, which are probably due to symmetric stretching of Zn−O and TM−O bonds in the tetrahedral coordination [75]. The lines at 636 cm^{-1} and 671 cm^{-1} are probably a mixture of two modes related with stretching along Zn−O bonds [76,77] and TM−O bonds [78], correspondingly. The modes $F2g(2)$ and $F2g(3)$ can be attributed to the vibrations of the octahedral groups [73,75–78].

Therefore, firstly, we can resume that the observed Raman spectra for wurtzite phases in TM-doped samples are compatible both with the described above our XRD data and literature sources. Secondly, as follows from the Table 2, the presence of iron-enriched
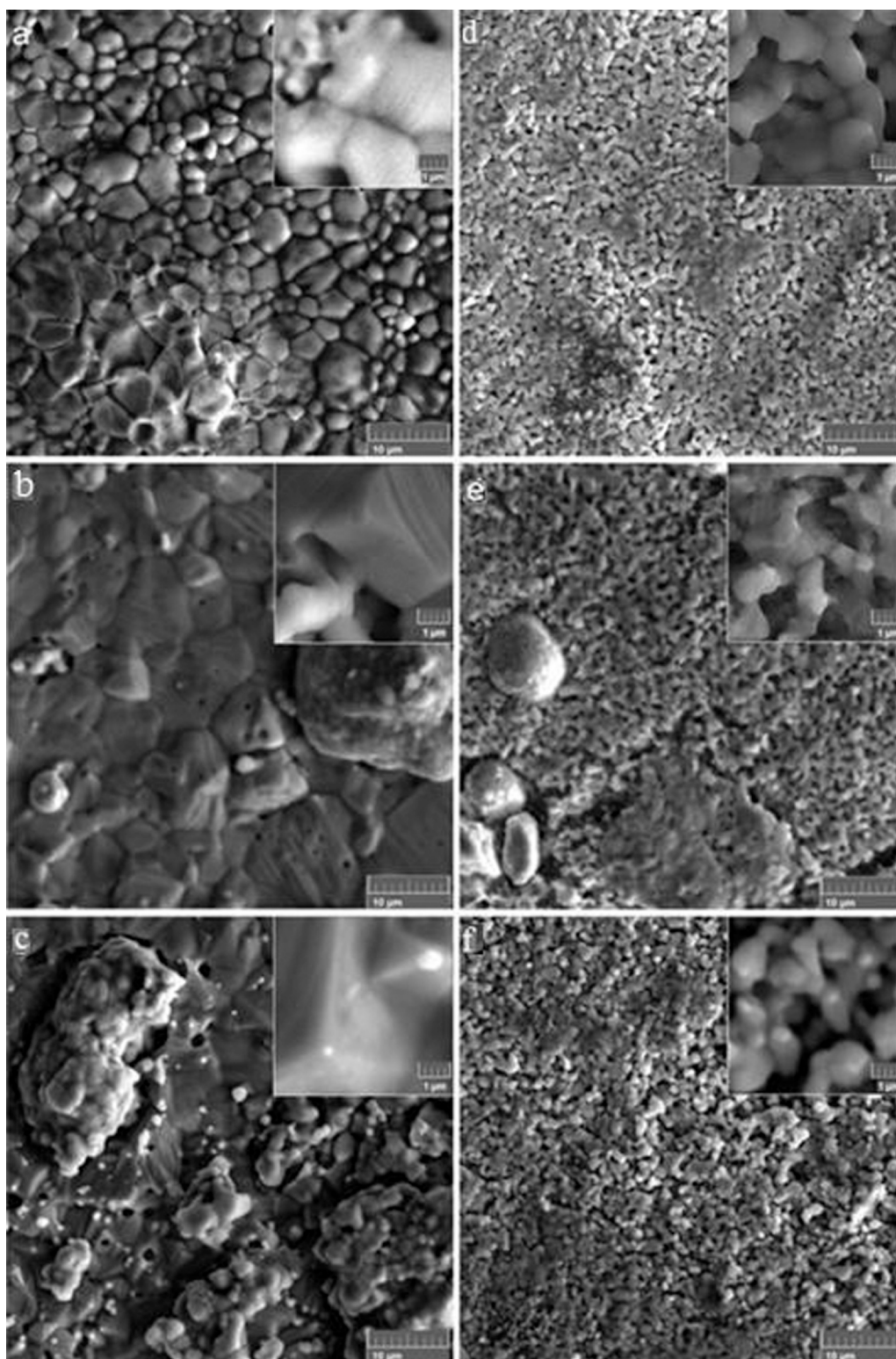
Fig. 3. Typical SEM images (marker is 10 micrometers) of the grain structure on the cleaved surface of ceramics $[(TM)_xO_y]_{10}(ZnO)_{90}$ obtained after two – (*a, b, c*) and one-stage (*d, e, f*) synthesis using CoO (*a, d*), FeO (*b, e*) and α-Fe$_2$O$_3$ (*c, f*) oxides as the doping agents. The Inserts in top right corners of pictures give the SEM images with higher magnification (marker is 1 micrometer).

precipitates with the ZnFe$_2$O$_4$ ferrite structure and/or residual Fe$_x$O$_y$ oxides increases the average iron content in samples up to 1–5 at% that is lower than the rated nominal concentrations z of Fe in ceramic samples $(ZnO)_z[(TM)_xO_y]_{1-z}$. It is logically to attribute this discrepancy to the fact that, most likely, some of iron atoms are not incorporated into ZnO lattice and does not form ZnFe$_2$O$_4$ and/or

Fe$_x$O$_y$ granules, segregating at grain boundaries [79] and/or internal surfaces of pores. Just by this reason they do not contribute to the extra lines of XRD patterns of Fe-doped samples.

To analyze additionally the magnetic status of the phases formed during the synthesis and annealing procedures in the studied composite ceramics doped with TM, we measured their magnetization
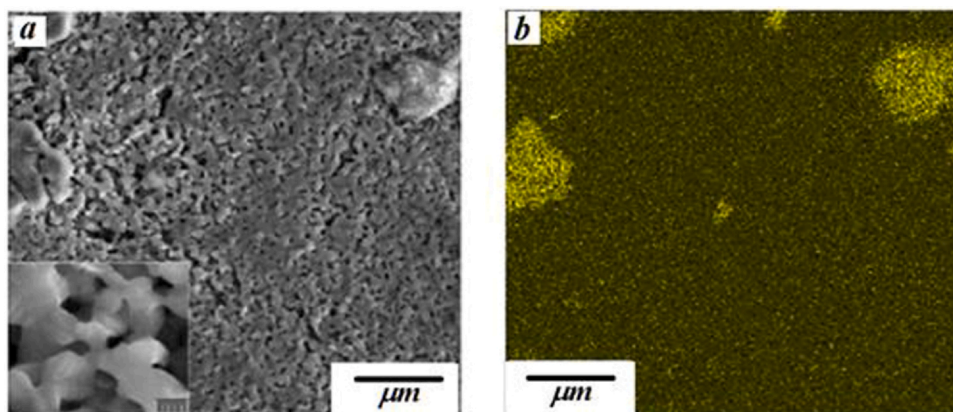
Fig. 4. Examples of SEM images (*a*) and EDX pattern of Fe distribution (*b*) in composite ceramics $(ZnO)_{90}(FeO)_{10}$-2 (Sample 6 in Table 2).

curves as well as the Mössbauer spectra (MS) for the samples containing iron ions (see, Figs. 9–11). MS spectra were measured both for initial powders before their compacting and also on powders prepared from pellets after one-step or two-step procedures of preparation.

The MS confirms the XRD, EDX and Raman data concerning the presence of secondary, enriched by iron precipitates in the studied ceramics. As follows from the recorded MS for the sample $(ZnO)_{90}(FeO)_{10}$, at room temperature a singlet of powder mixture (Fig. 9a) is transformed after sintering and annealing into doublet (with the isomeric shift IS = 0.35 mm/s and quadrupole splitting $\Delta = 0.34$ mm/s) corresponding to the paramagnetic $ZnFe_2O_4$ with a ferrite structure (Fig. 9b and c) [3,57]. We should note also that this doublet is observed on the Mössbauer spectra for all the studied $ZnO\text{-}Fe_xO_y$ ceramics in the whole investigated temperature range (20–300 K). Note, that both after one- and two-step preparation, the Mössbauer spectra of $(ZnO)_{90}(FeO)_{10}$ ceramic samples show one doublet corresponding to iron ions in charge state Fe^{3+}. It should be noted that the hyperfine parameters of the obtained phases do not depend on number of stages in synthesis procedure.

As can be seen from (Fig. 10a and b), Mössbauer spectra of both $(ZnO)_{90}(Fe_2O_3)_{10}$ and $(ZnO)_{90}(Fe_3O_4)_{10}$ ceramics also include mainly a nonmagnetic doublets, identical to that observed for $(ZnO)_{90}(FeO)_{10}$ ceramic samples. To identify the phase corresponding to this subspectrum (doublet), low-temperature MS studies of $(ZnO)_{90}(Fe_2O_3)_{10}$ ceramics were carried out, which allowed us to distinguish the superparamagnetic properties of the material from the paramagnetic ones. The low-temperature Mössbauer spectra in Fig. 11 for the ceramics, obtained by two-step preparation procedure, have shown that the decrease of temperature down to 20 K does not result to magnetic splitting of spectral lines, i.e. a nonmagnetic doublet still remains dominant (on –60%) and its hyperfine parameters are close to those observed at room temperature. In
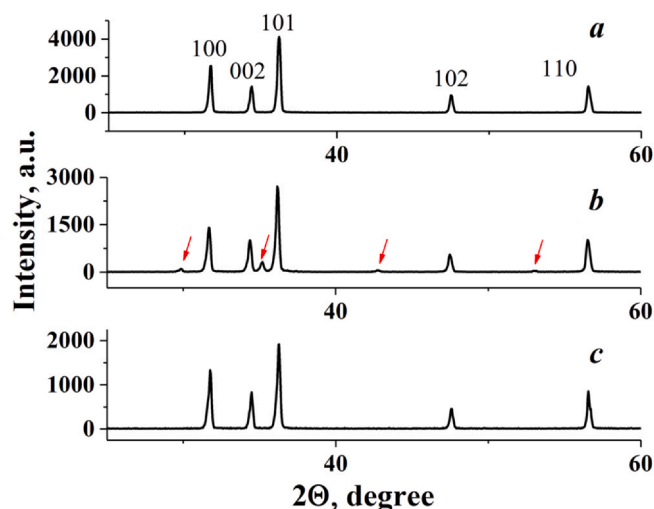

Fig. 6. Examples of typical XRD spectra in undoped ZnO (*a*) and composite ceramics $(ZnO)_{90}(FeO)_{10}$ (*b*) and $(ZnO)_{90}(CoO)_{10}$ (*c*). In Fig. 6a the Miller indices for the wurtzite lattice of zinc oxide are shown by black color. Red arrows in Fig. 6b show the observed additional lines corresponding to the ferrite phase $(ZnO)_z(Fe_xO_y)_{1-z}$ or residual iron oxides Fe_xO_y.

other words, the conservation of the doublet at low temperatures confirms the paramagnetic character of the corresponding phase. In accordance with [80], the $ZnFe_2O_4$ zinc ferrite possesses the paramagnetic properties and similar parameters of Mössbauer spectra. As is seen from Figs. 2 and 4, the formation of this phase is in agreement with the data of EDX method and Raman spectra.

We observed in the local structure of $(ZnO)_{90}(Fe_3O_4)_{10}$ composite the presence of the magnetically split sextet with isomeric shift
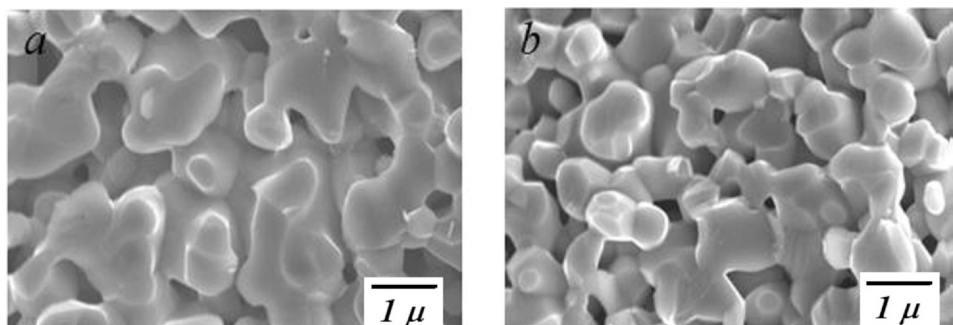

Fig. 5. Examples of SEM images in ceramic tablets $(ZnO)_{90}(CoO)_{10}$ after 1st stage (*a*, sample 18) and 2nd stage (*b*, sample 19) of sintering procedures.

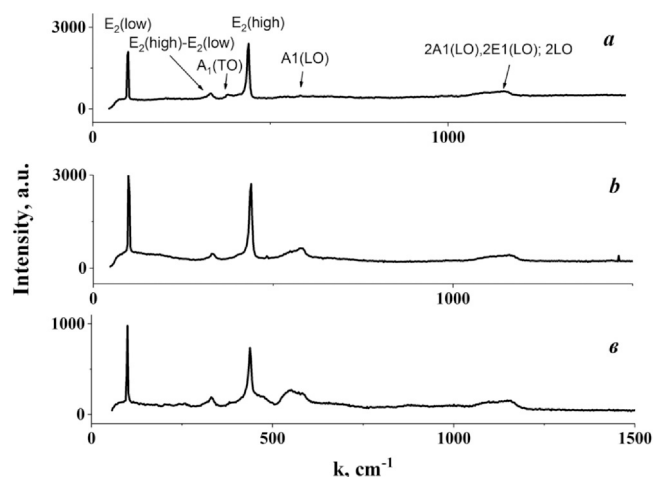**Fig. 7.** Examples of Raman spectra in undoped ZnO (*a*) and in samples 12 $(ZnO)_{90}(FeO)_{10}$-2 (*b*) and 19 $(ZnO)_{90}(CoO)_{10}$-2 (*c*) in the regions where only the wurtzite phase exists.
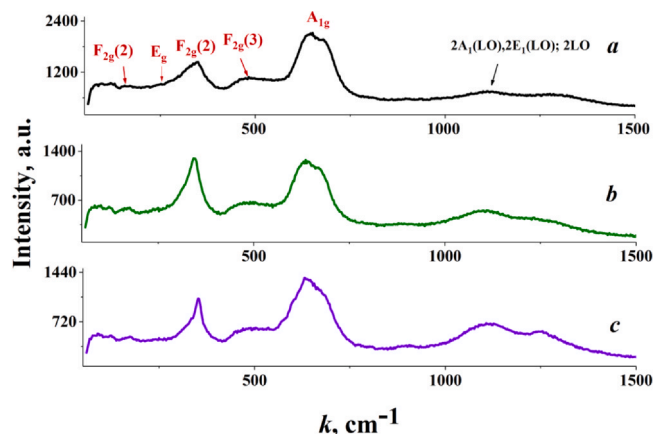

Fig. 8. Examples of Raman spectra for the Fe-enriched phase precipitates with micronic sizes in the iron doped composite ceramics, obtained by two-stage synthesis method: $(ZnO)_{90}(FeO)_{10}$ (*a*), $(ZnO)_{90}(Fe_2O_3)_{10}$ (*b*) and $(ZnO)_{90}(Fe_3O_4)_{10}$ (*c*).

$IS = 0.37$ mm/s and characteristic magnetic field $B_{eff} = 51.7$ T. Its contribution to Mössbauer spectrum was about 23% that is in agreement with the results of paper [43]. Its hyperfine parameters coincide with the corresponding parameters of the MS for the initial powder mixture used for the ceramics preparation, namely Fe^{3+}-containing oxide. Probably, this sub-spectrum characterizes the local configurations of Fe ions in the large iron-rich microparticles shown in SEM and EDX images in Figs. 2 and 4.

To confirm the above-described magnetic state of the observed phases in the $(ZnO)_{90}(Fe_xO_y)_{10}$ ceramics, we have analyzed additionally magnetization curves μ(B) in the temperature range of 5–300 K for the two-stage samples $(ZnO)_{90}(\alpha-Fe_2O_3)_{10}$-2 (sample 13) and $(ZnO)_{90}(Fe_3O_4)_{10}$-2 (sample 14), which showed differences in their local ordering according to Mössbauer data. According to XRD, Raman and MS data, the $(ZnO)_{90}(\alpha-Fe_2O_3)_{10}$-2 sample demonstrates a large amount of Fe^{3+}-oxide (probably hematite $\alpha-Fe_2O_3$) and the least amount of $ZnFe_2O_4$ ferrite.

As can be seen from Fig. 10c, the $(ZnO)_{90}(\alpha-Fe_2O_3)_{10}$-2 sample, prepared by two-stage technology, demonstrates paramagnetic shape of magnetization curves μ(B) at the temperature range 150–300 K and remains predominantly paramagnetic at lower temperatures 10–50 K. Such behavior is due to paramagnetic character of the ferrite $ZnFe_2O_4$ in such ceramics. When we cool down the sample $(ZnO)_{90}(\alpha-Fe_2O_3)_{10}$-2 below 50 K, its μ(B) curve

demonstrates hysteresis with the coercivity H_C of the order of 350–450 Oe. This may be caused by transition of $ZnFe_2O_4$ to the antiferromagnetic state that typically takes place at 10 K. Note also, that, the low-field magnetization and the magnetic susceptibility dμ/dB of the sample increases when temperature decreasing.

The sample $(ZnO)_{90}(Fe_3O_4)_{10}$-2 demonstrates more complicated character of μ(B) curve (Fig. 10d). This curve clearly shows two components in the whole temperature range [45]. The first component is identical to that in μ(B) for the sample $(ZnO)_{90}(\alpha-Fe_2O_3)_{10}$-2 in Fig. 10c, i.e. it characterizes the $ZnFe_2O_4$ sub-system. According to MS data, this component includes more than 70% of the iron-containing phases. The second component of μ(B) curve for ceramic sample $(ZnO)_{90}(Fe_3O_4)_{10}$-2 is different from the previous $(ZnO)_{90}(\alpha-Fe_2O_3)_{10}$-2 sample in Fig. 10c. It shows a hysteresis loop with high magnetic susceptibility at low fields and non-zero coercivity (up to 300 Oe) even at room temperature that is compatible with the results of [81]. The latter is supposed to be hematite $\alpha-Fe_2O_3$ revealed in this ceramic by Mössbauer spectroscopy (compare also with [81]), which possesses weak ferromagnetic properties at room temperature.

Summarizing the results for the described above structure and magnetic state of the studied ceramics, we can resume the following. The ZnO < Co > pellets are solid solutions for all the studied compositions and contain granules with sizes of 1–2 μm. The main volume of the ZnO < Fe > samples is occupied by the wurtzite phase $Zn_{1-\delta}Fe_\delta O$ with granules of submicron sizes where iron atoms are dissolved in concentrations $0.66 \le \delta \le 0.87$ at%. At the same time, as follows from XRD, RS, EDX and Mossbauer spectroscopy and magnetometry as well, the studied Fe-doped ceramic samples with initial weight concentrations of iron of more than 3–5 wt% contain iron-rich secondary phases of ferrite $ZnFe_2O_4$ (with the perovskite structure) and the residual cubic oxides Fe_xO_y.

4. Temperature dependences of resistivity, Hall effect and Seebeck effect

This section presents and discusses the temperature dependences of resistivity, as well as Hall and Seebeck coefficients for the studied ceramic samples depending on the preparation technology (one- or two-stage), type of doping agents $(TM)_xO_y$ and phase structure.

Fig. 12 shows the influence of doping on temperature dependences of normalized resistivity ρ(T)/ρ(300 K) for some ceramic samples $(ZnO)_z[(TM)_xO_y]_{1-z}$ prepared by both one- and two-step synthesis technologies. As follows from this figure, the studied samples can be divided provisionally into two groups by their the character of their ρ(T) dependences around room temperature in Arrhenius scale. For the Fe-doped and mostly high-resistive ceramics, curves Lg [ρ(T)/ρ(273 K)]-(1/T) are linear for some samples prepared by one-step technology (curves 5 and 8) and all two-step ones (curves 11–15). As is seen from Tables 3 and 4, the linear parts of Arrhenius curves at 200–300 K show very similar slopes giving activation energies of conductivity close to $\Delta E_\sigma = (0.36 \pm 0.02)$ eV.

The Lg [ρ(T)/ρ(273 K)]-(1/T) dependences for the second group, which include the mostly low-ohmic ceramic samples, show the so-called "sliding" (temperature dependent) ΔE_σ values below 200–250 K in Fig. 12. As follows from Tables 3 and 4, they refers to the undoped ZnO ceramic samples (curves 1 and 2) and also to some doped samples $(FeO)_{10}(ZnO)_{90}$-1, $(CoO)_{10}(ZnO)_{90}$-1 and $(CoO)_{10}(ZnO)_{90}$-2 (curves 5, 18, 19, accordingly). Note also that one-step sample 5 formally belongs to both groups (to the first at $T > 200$ K and to the second at temperatures below 200 K). The values of "sliding" ΔE_σ decrease upon cooling and does not exceed 0.05–0.09 eV at the studied temperature range. Such behavior is attributed very often by 2 reasons. The first reason is hopping of electrons by the localized states formed either in band gap or in
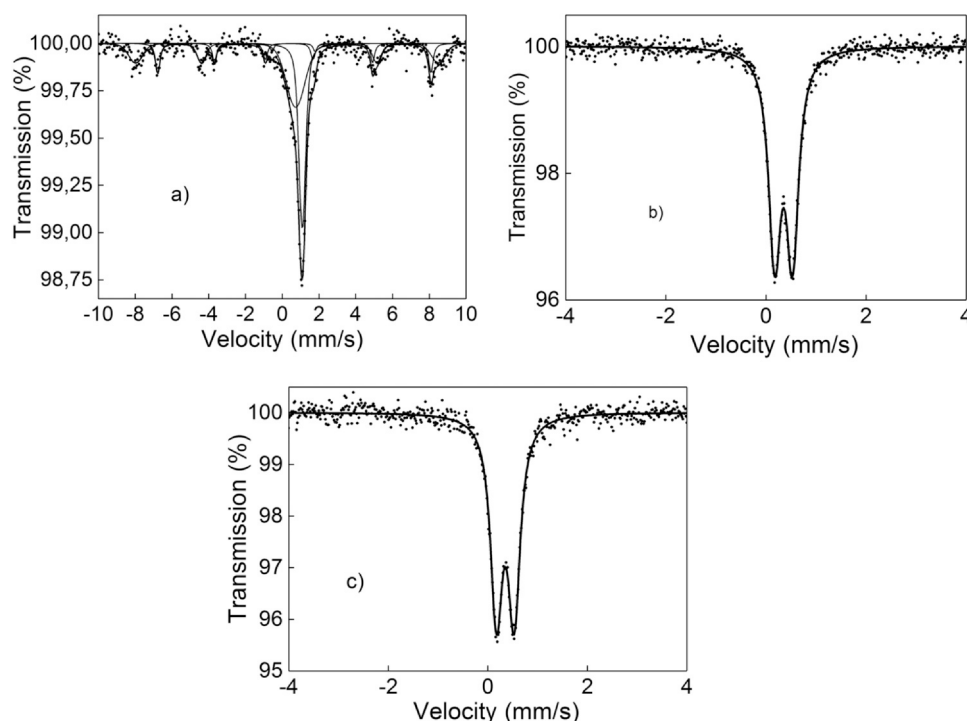
Fig. 9. The examples of Mossbauer spectra for the initial $(ZnO)_{90}(FeO)_{10}$ powder mixture (a) and corresponding composite ceramics $(ZnO)_{90}(FeO)_{10}$ after one-step (b) and two-step (c) preparation technology.

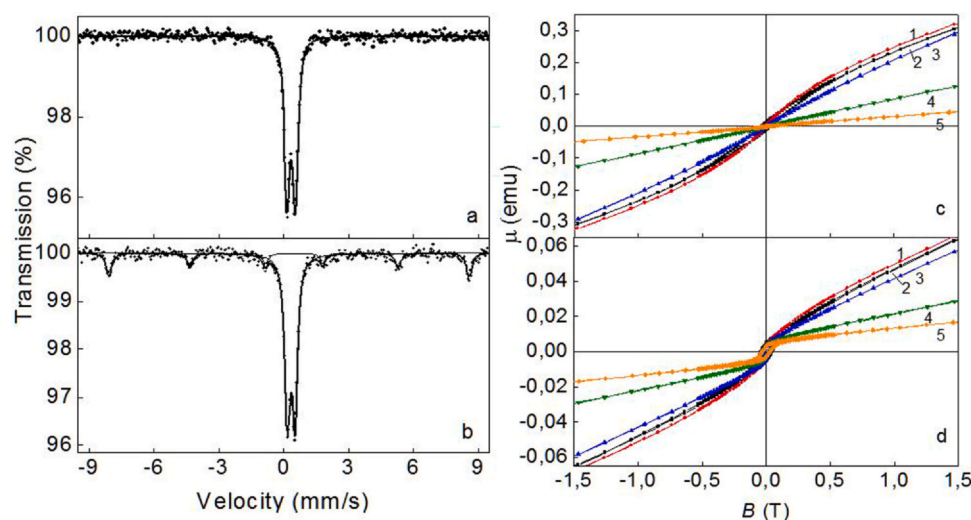**Fig. 10.** Mössbauer spectra (a, b) and magnetization curves (c, d) of the composite ceramics $(ZnO)_{90}(Fe_2O_3)_{10}$-2 (a, c) and $(ZnO)_{90}(Fe_3O_4)_{10}$-2 (c, d) prepared by two-step technology: 1 – 5 K, 2 – 10 K, 3 – 50 K, 4 – 150 K, 5 – 300 K.

band-tails of C(V)-bands due to disordering of semiconducting material (see. [80–86]). The second reason ascribes this behavior to the presence of the so-called Large-Scale Potential Relief (LSPR) in heterogeneous or strongly disordered and high-ohmic semiconductors. In our case, the formation of LSPR can be conditioned either by inhomogeneous distribution of impurities/defects in wurtzite phase $Zn_{1-\delta}(TM)_{\delta}O$ or multi-phase structure of some of ceramic samples. To clarify this issue, we measured temperature dependences of Hall constant $R_H(T)$ and Seebeck coefficient $S(T)$ in some of $(ZnO)_z$ $[(TM)_xO_y]_{1-z}$ samples. Unfortunately, we could make measurements of low-temperature $R_H(T)$ only in the mostly low-resistive samples.

To make a relative comparison of the influence of doping with cobalt or iron on the electrical transport properties in the $(ZnO)_z$ $[(TM)_xO_y]_{1-z}$ composite ceramics, we measured the temperature

dependences of the Seebeck coefficient below 300 K for 3 ceramic samples – the undoped zinc oxide (sample 1), $(FeO)_{10}(ZnO)_{90}$-1 (sample 5) and $(CoO)_{10}(ZnO)_{90}$-1 (sample 18). For convenience of comparison, these results are shown in Fig. 13 in normalized form $S(T)/S(273\,K)$. Note that the used in this experiment doped samples were prepare by a one-stage synthesis procedure. Since transition elements in doping agents (CoO and FeO) were present only in the form of doubly charged ions, it can be expected that in these doped ceramics, cobalt and iron replaced only zinc ions in the wurtzite lattice. We also recall that the Co-doped ceramics were in the form of solid solutions (with wurtzite lattice), whereas the Fe doping shown the presence of a secondary (mostly ferritic) phase.

Let us consider the features of $S(T)/S(273\,K)$ dependences in zinc oxide in the range 4–300 K before and after ZnO doping with iron or
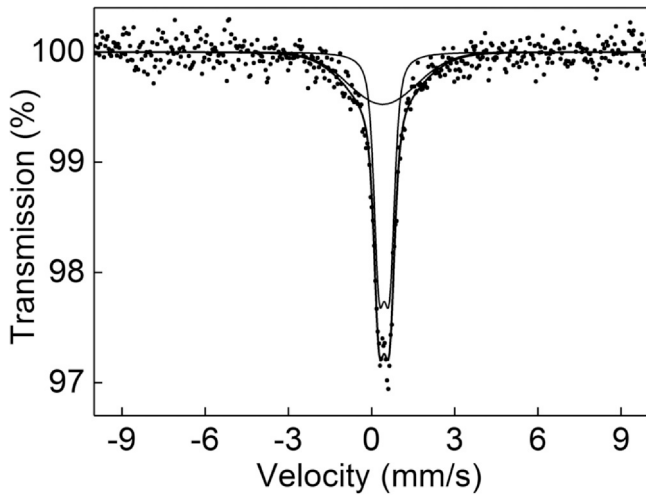
Fig. 11. Mössbauer spectrum of composite ceramics $(ZnO)_{90}(\alpha\text{-}Fe_2O_3)$, prepared by the two-step technology, which was measured at 20 K.
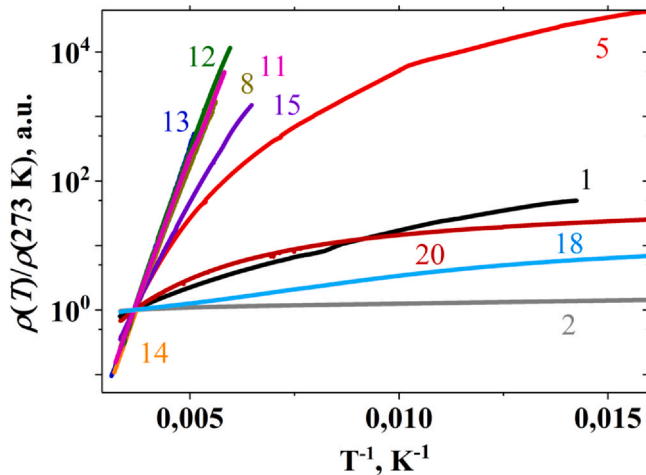

Fig. 12. Temperature dependences of the resistivity $\rho(T)/\rho(273\,K)$ in normalized Arrhenius scale for the undoped (1, 2) and doped (5, 8, 11–14, 18, 19) ceramic samples $(ZnO)_z[(TM)_xO_y]_{1-z}$, prepared by the one-step (1, 2, 5, 18) and two-step (8, 11–14, 19) synthesis procedures. The numbers near curves correspond to the samples in Table 1.

cobalt, and compare it with the temperature dependences of the resistivity and Hall coefficient. As follows from Fig. 13, the first feature of the $S(T)/S(273\,K)$ curves is that at temperatures below 20–30 K it is linear for samples undoped (curve 1), Fe-doped (curve 5) and Co-doped (curve 18) samples. In so doing, for the iron doped sample 5, the $S(T)$ in the whole range of the studied temperatures is

always lies negative, whereas for the samples 1 and 18 negative S change its sign on positive below 20–30 K (see, insets in Fig. 13).

The second feature is the difference of $S(T)$ law character at low and high temperatures and the influence of the type of doping on its progress. As can be seen from Fig. 13a, at low temperatures the behavior of $S(T)/S(273\,K)$ for the undoped ZnO (curve 1 in Fig. 13a) is linearized in Arrhenius coordinates, that possibly may indicate the activation character of carrier transport with an activation energy of about 9–10 meV. At high temperatures, the $S(T)/S(273\,K)$ dependences become linear in double logarithmic coordinates with slopes of the order of 0.5, that is especially clearly seen for sample 5 (Fig. 13a). The latter corresponds to the well-known Zvyagin's relation for $S(T)$ in strongly disordered semiconductors [87].

The third feature is that the addition of CoO increases the S of zinc oxide much weaker compared to the sample doped with iron. So, for example, in the low-temperature range the value of S in ZnO-based ceramics, when doping with cobalt, increases only slightly, while when doping with iron in the form of FeO, it increases much more strongly (see inset in Fig. 13a). Possible reasons in different influences of Fe and Co doping on S values of ZnO ceramic samples in context of the specificity of behavior of their $S(T)$, $\rho(T)$ and $R_H(T)$ curves will be described below.

Our experiments have shown that Hall constant R_H, calculated from relation

$$R_H = \frac{r}{ne},\qquad(2)$$

has shown negative sign for all of the measured samples at temperatures $T > 100\,K$. Here r is a constant, which depends on mechanism of carrier scattering and, accordingly [94], tends to unity in strong magnetic fields. As is seen from Table 3, in the studied samples the room temperature n values lie in the range of $(8 \times 10^{18}\text{-}3 \times 10^{22})\,m^{-3}$. In so doing, Fig. 14 indicates two contributions to $n(T)$ dependences, where their Arrhenius plots can be fitted by linear dependences, with different slopes (ionization energies). As is follows from Fig. 14, these dependences have smaller slopes ΔE_1 at $T < 150\,K$ and larger slopes ΔE_2 at $T > 200\,K$, accordingly. We attribute such behavior of Arrhenius Lg $n(1/T)$ curves to the formation of two types of defect centers with different ionization energies ΔE_1 and ΔE_2 (see, Table 3) in the prepared ceramic samples.

The temperature dependences of Hall mobility $\mu_H(T)$ of carriers for some of mostly low-resistive samples were estimated by relation [73].

$$\mu_H = R_H/\rho,\qquad(3)$$

where:

$$\rho(T) = \rho_0 \exp[-(\Delta E_\sigma/kT).\qquad(4)$$

Here ΔE_σ – energy of conductivity activation, which is close to impurity ionization energy in a standard band conduction model.

Table 3

Values of ionization energies ΔE_1 and ΔE_2 estimated from $n(T)$, conduction activation energies ΔE_σ estimated from $\rho(T)$ as well as the exponent k in Eq. (4) calculated from temperature dependences of the Hall mobility μ_H for the undoped ZnO (samples 1, 2) and doped (samples 12, 13,15, 18–20) ceramics.

№	Sample	n, m^{-3} ($T = 300\,K$)	ΔE_1, eV ($T < 150\,K$)	ΔE_2, eV ($T > 200\,K$)	ΔE_σ, eV	μ_H, m^2/V s ($T = 300\,K$)	Exponent k in the ratio (3) for $T > 200\,R$
1	ZnO-A	$9.3 \cdot 10^{20}$	0.009	–	0.05	$1.83 \cdot 10^{-4}$	-2,10
2	ZnO-B	$1.9 \cdot 10^{21}$	0.004	–	0.05	$7.38 \cdot 10^{-5}$	0.71
5	$(ZnO)_{90}(FeO)_{10}$-1	$5.73 \cdot 10^{21}$	–	0.09	0.26	$8.09 \cdot 10^{-4}$	-3.2
8	$(ZnO)_{90}(Fe_2O_3)_{10}$-1	$5.97 \cdot 10^{21}$	–	0.15	0.34	$2.04 \cdot 10^{-3}$	-4.3
12	$(ZnO)_{90}(FeO)_{10} - 2$	$1.6 \cdot 10^{19}$	0.004	0.306	0.36	$4.93 \cdot 10^{-4}$	-2.9
13	$(ZnO)_{90}(Fe_2O_3)_{10} - 2$	$8.2 \cdot 10^{18}$	–	0.241	0.37	$2.38 \cdot 10^{-4}$	-2.5
15	$(ZnO)_{90}(FeO+Fe_2O_3)_{10}$-2	$1.9 \cdot 10^{21}$	0.014	0.164	0.24	$7.38 \cdot 10^{-5}$	-2.7
18	$(ZnO)_{90}(CoO)_{10}$-1	$4.12 \cdot 10^{22}$	0.005	0.061	0.02	$3.24 \cdot 10^{-5}$	0.3
20	$(ZnO)_{95.0}(CoO)_{5.0}$-1	$6.45 \cdot 10^{20}$	0.006	0.070	0.009	$4.58 \cdot 10^{-4}$	-1.6

Table 4
The main electrical parameters and Seebeck coefficient measured at room temperature in the studied samples $(ZnO)_z[(TM^*)_xO_y]_{1-z}$.

№*	Samples	ρ_{300}, Ω m	R_H (300 K), m³/C	S_{300}, μV/K	$P_{300} = S^2/\rho$, W/K² m
1	ZnO-A	$3.67\cdot10^1$	0.00671	385 ± 10	$4.04\cdot10^{-9}$
2	ZnO-B	$2.98\cdot10^{-1}$	0.00692	229 ± 15	$1.76\cdot10^{-7}$
3	$(ZnO)_{98}(FeO)_2$-1	$7.69\cdot10^{-3}$	–	595 ± 25	$4.60\cdot10^{-5}$
4	$(ZnO)_{95}(FeO)_5$-1	$5.70\cdot10^{-3}$	–	609 ± 26	$6.51\cdot10^{-5}$
5	$(ZnO)_{90}(FeO)_{10}$-1	$1.34\cdot10^0$	$1.09\cdot10^{-3}$	735 ± 15	$4.77\cdot10^{-7}$
6	$(ZnO)_{98}(Fe_2O_3)_2$-1	$1.70\cdot10^{-2}$	–	409 ± 37	$9.87\cdot10^{-6}$
7	$(ZnO)_{95}(Fe_2O_3)_5$-1	$1.13\cdot10^2$	–	400 ± 4	$1.41\cdot10^{-9}$
8	$(ZnO)_{90}(Fe_2O_3)_{10}$-1	$9.71\cdot10^0$	$1.04\cdot10^{-3}$	765 ± 5	$6.03\cdot10^{-8}$
9	$(ZnO)_{98}(FeO+Fe_2O_3)_2$-1	–	–	582 ± 149	–
10	$(ZnO)_{95}(Fe_3O_4)_5$-1	–	–	592 ± 50	–
11	$(ZnO)_{90}(Fe_3O_4)_{10}$-1	$2.86\cdot10^5$	–	955 ± 55	$3.19\cdot10^{-7}$
12	$(ZnO)_{90}(FeO)_{10}$-2	$7.89\cdot10^2$	$3.89\cdot10^{-1}$	603 ± 43	$4.61\cdot10^{-10}$
13	$(ZnO)_{90}(Fe_2O_3)_{10}$-2	$3.18\cdot10^3$	$7.58\cdot10^{-1}$	299 ± 28	$2.83\cdot10^{-11}$
14	$(ZnO)_{90}(Fe_3O_4)_{10}$-2	$6.12\cdot10^2$	–	–	–
15	$(ZnO)_{90}(FeO+Fe_2O_3)_{10}$-2	$4.37\cdot10^1$	$6.71\cdot10^{-3}$	835 ± 26	$1.6\cdot10^{-8}$
16	$ZnO)_{98}(CoO)_2$-1	$1.70\cdot10^{-2}$	–	409 ± 37	$9.87\cdot10^{-6}$
17	$ZnO)_{95}(CoO)_5$-1	$1.13\cdot10^2$	–	400 ± 4	$1.41\cdot10^{-9}$
18	$ZnO)_{90}(CoO)_{10}$-1	$4.67\cdot10^0$	$1.51\cdot10^{-4}$	386 ± 8	$3.19\cdot10^{-8}$
19	$ZnO)_{90}(CoO)_{10}$-2	$5.1\cdot10^0$	$2.0\cdot10^{-4}$	580 ± 20	
20	$(ZnO)_{95.0}(CoO)_{5.0}$-1	$2.11\cdot10^1$	$9.67\cdot10^{-3}$	363 ± 27	$6.24\cdot10^{-9}$
21	$(ZnO)_{99.5}[(CoO)_{50}^*(ZnO_{50})]_{0.5}$-1	$4.17\cdot10^{-3}$	–	350 ± 15	$2.94\cdot10^{-5}$

**Numbers 1 and 2 in the samples labeling after chemical formula in the second column denote the same as in Tables 1 and 2.
* TM – transition metals (Fe or Co)

We can see from Fig. 15 the following specific features. Firstly, at temperatures 150 < T < 300 K $\mu_H(T)$ curves are characterized by relatively low values of mobility with power-law temperature dependences.

$$\mu_H(T) \sim T^k. \tag{5}$$

As is seen in from Table 3, at $T \geq 200$ K the exponent k in (5) is close to the value (−2.1) for the undoped sample 1 and to the value (−2.3 ± 0.6) for the homogeneous ceramic samples prepared by two-step synthesis (samples 12, 13, 15). We can attribute such behavior to the scattering of electrons on the ionized defects and/or impurities.

Note also, that, as is seen from Table 4, the samples 2 and 20 show small positive values of k exponent in (5) which indicate possible contribution of another mechanism of scattering. We can attribute this fact to the scattering of electrons by phonons. Secondly, below 200 K, the negative exponent k for the doped samples strongly falls down by modulo with the temperature decrease giving physically unreasonable values (see points below 200 K for curves 5, 12, 13, 15 and 19 in Fig. 15). Below we discuss possible reasons of such behavior.

Let us discuss the above-described carrier transport properties in the studied samples. As follows from Table 4 and Fig. 14a, at temperatures below 150 K, in the undoped zinc oxide (samples 1 and 2) and some doped samples (12, 15, 18, 20) the obtained values of

ionization energies ΔE_1 are close to those observed in literature [84–86] for shallow donors in wurtzite lattice. The most of researchers attribute shallow centers to such intrinsic defects as oxygen vacancies and/or interstitial zinc ions [84–86].

At high temperatures, the estimated ΔE_2 and ΔE_σ values for the doped samples indicate the formation of deep donors with energy levels 0.24–0.37 eV, see Table 4 and Fig. 14. Note also, that some of ΔE_σ values in iron-doped ceramics for the temperature range of 150–300 K, significantly exceed those known from the literature. For example, for polycrystalline ZnO films with an iron content of 0.2 wt % authors of paper [86] observed $\Delta E_\sigma = 0.35 \pm 0.02$ eV. Note also that a number of authors present more deep centers with the ionization or conduction activation energies of about 0.15–0.4 eV even in the undoped zinc oxide [66,89–91]. They attributed these deep levels either to the formation of an impurity band due to doping, which is overlapping with bottom of C-band, and/or "tails" of localized states in C-band due to dopants [92,93] or intrinsic donor-like defects [66,90,91]. Actually, when producing of ceramics on air, the increase of oxygen atoms can result in an increase of zinc vacancies (Zn_v^{2-}), which, according to [91], will play a role of deep donors. Moreover, this formation of Zn_v^{2-} vacancies can be enhanced by the departure of a significant part of zinc atoms on the formation of $ZnFe_2O_4$ ferrite particles that were observed in our Fe-doped samples. On the other hand, the replacement of a part of zinc atoms by iron atoms in the wurtzite lattice, as well as the increase of concentration of oxygen
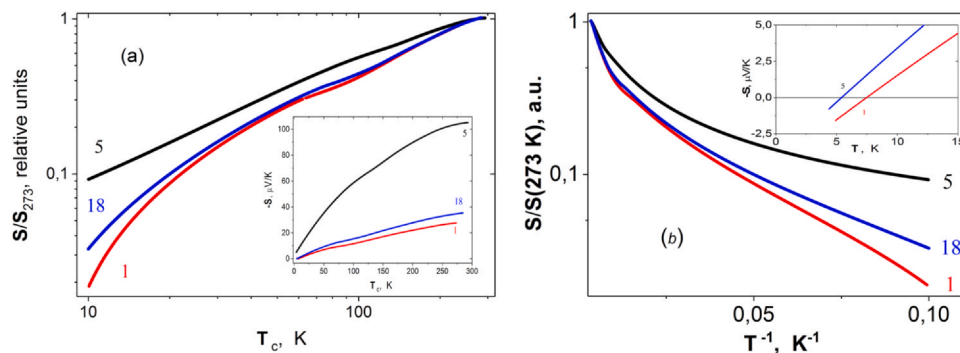

Fig. 13. Temperature dependences of the normalized Seebeck coefficient $S(T)/S(273$ K) in double logarithmic (a) and in Arrhenius (b) scales. Insert (a): $S(T)$ in linear scale. Insert (b): $S(T)$ in linear scale below 15 K.
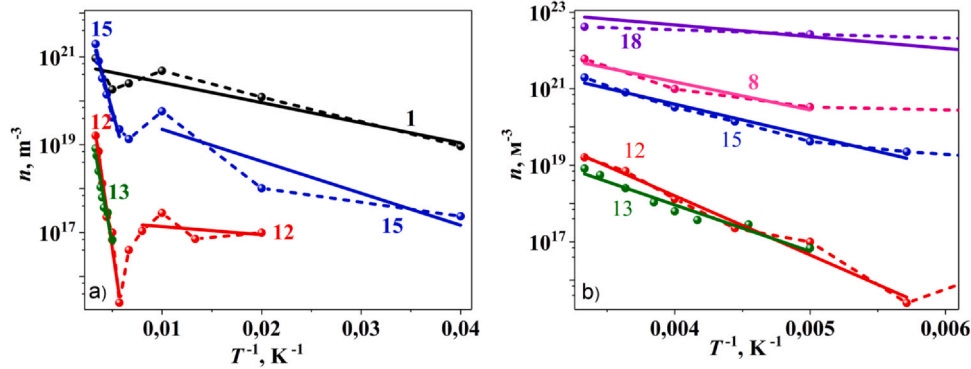
Fig. 14. Examples of temperature dependences of electron concentration $n(T)$ in Arrhenius scale for the whole temperature rang (*a*) and $T > 100$ K (*b*) for the samples 1, 8, 12, 13, 15, 18 in Table 3. Points, linked by the dashed lines, show the experimental results. Solid straight lines are approximations of linear parts of Lg $n(1/T)$ dependencies at low and/or high temperatures.
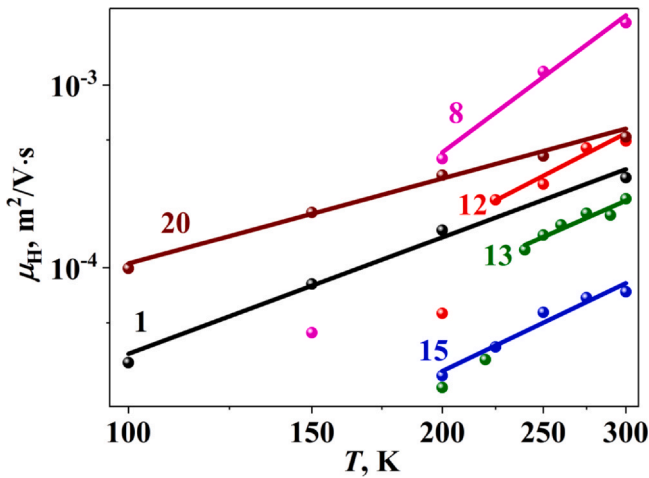

Fig. 15. Temperature dependences of the Hall mobility $\mu_H(T)$ in logarithmic scale for the samples 1, 8, 12, 13, 15 and 20.

atoms during the pre-sintering and post-sintering annealing on air can also lead to the formation of Fe-O complexes. In such a case, we can attribute the observed deep level in the doped ZnO < Fe > ceramics to the formation of these complexes. Note also that paper [85] attributes deep centers with ΔE_σ about 0.34 eV to antisite defect O_{Zn} (oxygen in Zn-sublattice). Therefore the nature of deep centers in undoped and Fe(Co)-doped ZnO ceramics needs more research.

As was noted above, the $\rho(T)$ and $S(T)$ dependences in the Arrhenius scale in Figs. 12 and 13b for the samples 1, 2, 5, 18, 20 were characterized by the so-called "sliding" activation energy, which decreased when cooling. In literature, this is usually attributed to either variable range hopping (the so-called VRH regime [92,93]) of electrons by localized states or the presence of "tails" of localized states due to strong disordering, as well as Large-Scale Potential Relief (LSPR) formation due to non-uniform distribution of impurities and defects. In case of VRH carrier transport, temperature dependences of resistivity are usually described by the well-known Mott relation [92,93]:

$$\rho(T) = \rho_{01} \cdot \exp[-(T_{01}/T)^\alpha], \qquad (6)$$

where in bulk semiconductors the exponent α is close either to 0.25 for the Mott mechanism or to $\alpha = 0.5$ for Shklovsky-Efros VRH regime. Here, ρ_{01} and T_{01} are the characteristic parameters of the corresponding VRH process, which are dependent on the density of localized states and the electron localization radii of defects.

In nonhomogeneous semiconductors with strong LSPR the temperature dependences of the electrical resistivity are described by the relation.

$$\rho(T) = \rho_{03} \exp[-(\Delta E(T)/kT), \qquad (7)$$

where: $\Delta E(T)$ – activation energy which do not match with energy of impurities ionization as in a standard band conduction model. Accordingly [80–84], $\Delta E = (E_p - E_F)$, where E_F and E_p are Fermi energy and the percolation level, accordingly, which are dependent on temperature.

In order to understand which of the above mechanisms describes our experimental data most correctly, we used the procedure for replotting of the $\rho(T)$ dependences in different scales in accordance with relations (5) and (6).

To prove the agreement (or disagreement) of low-temperature carrier transport with VRH behavior, we presented experimental $\rho(T)$ curves for the samples of the above-mentioned second group with the changing activation energies in the so-called Mott coordinates Lg (ρ)-(1/T)$^\alpha$. As is seen, Mott curves in Fig. 16 can be described by two straight lines with different slopes. To resolve correctly, which of the laws (Mott or Shklovsky-Efros) fits better the observed experimental $\rho(T)$ dependences, we performed the appropriate approximation procedure. In accordance with formula (6), this procedure uses α, ρ_{01} and T_{01} as fitting parameters. In the temperature range below 15 K, the least errors gave relation (6) with $\alpha = 0.25$ for the samples contained only wurtzite phase – undoped ZnO (curves 1 and 2) and Co-doped ceramics $Zn_{1-\delta}Co_\delta O$. In particular, at these temperatures, the optimized fitting parameters for Mott law were $\rho_{01} = 719$ Ω m and T_{01} = 17 K (samples 1); $\rho_{01} = 65$ Ω m and $T_{01} = 20$ K (samples 18); ρ_{01} = 656 Ω m and $T_{01} = 16$ K (sample 20); $\rho_{01} = 65$ Ω m and $T_{01} = 18$ K (sample 18); $\rho_{01} = 0.65$ Ω m and $T_{01} = 15$ K. At higher temperatures 20 < T < 40 K, the optimized values for the samples 1 and 20 were $\alpha = 0.5$ that corresponded to Sklovski-Efros law. Other fitting parameters were equal to $\rho_{02} = 76$ Ω m and $T_{02} = 72$ K for the sample 1 and to $\rho_{02} = 73$ Ω m and $T_{02} = 70$ K for the sample 1.

For the sample 5 in Fig. 16, procedure of fitting has given bad result.

Comparison of $\rho(T)$ presented in Fig. 16 indicates good agreement with the known literature data [66,85,92,94]. For example, for ZnO single crystals doped with intrinsic defects (like interstitial zinc atoms and/or oxygen vacancies) paper [85] shows that combination of Mott-like hopping and standard conductivity by C-band, which exhibits shallow and deep donor levels with an ionization energies of the order of 0.05 eV and 0.25 eV, accordingly.

Note, that in the temperature range between 50 K and 200 K all the samples in Fig. 16 with moderately high resistance display transition to another type of $\rho(T)$ dependence, describing by relation
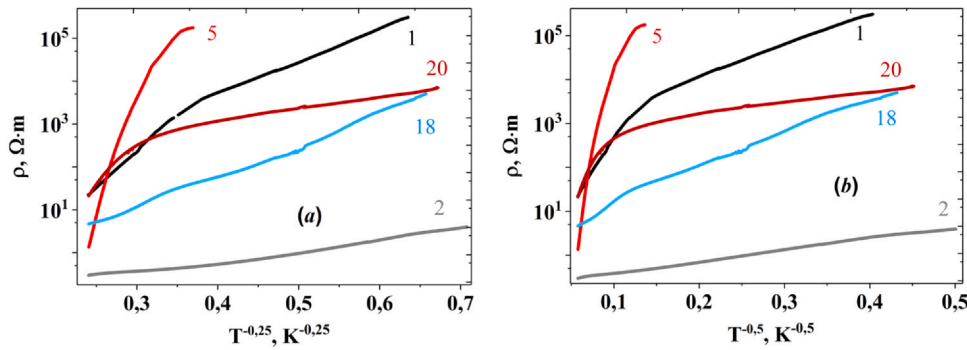
Fig. 16. Temperature dependences of the electrical resistance in the undoped zinc oxide (samples 1 and 2) and the doped $(ZnO)_z[(TM)_xO_y]_{1-z}$ ceramics (samples 5, 18, 20) in Mott coordinates $\log(\rho) - T^{-0,25}$ (a) and $\log(\rho) - T^{-0,5}$ (b).

(7). Accordingly [80–84], such form of $\rho(T)$ dependence confirms the formation of LSPR resulting in the appearance of percolation conductivity [91,92], when the percolation level E_p in relation (7) approaches the Fermi level E_F. Note that the LSPR formation is also confirmed by some additional arguments. Firstly, the temperature dependence of Seebeck effect in Fig. 12 in the studied sample 1, 5, 18 at $T > 100$ K where $S(T)$ follows to Zvyagin relation (see, above). Secondly, the described above behavior of the temperature dependences of the electron mobility (strong increase of k exponent in (4) with the temperature lowering) and immeasurability of Hall effect below 200 K. Therefore, the formation of LSPR in the studied samples can be attributed to the growth of the inhomogeneity of ceramic samples because of the strong disordering due to the presence of both intrinsic defects (in undoped ZnO) and TM doping (in samples 5, 15, 18, 20) [80–84].

As is seen from Figs. 12 and 16, the increase of temperature above 150–200 K results in transition of $\rho(T)$ for some doped ceramic samples and undoped sample 1 to usual band conductivity described by relation (4) [83,88] with activation energies ΔE_σ close to 0.35–0.37 eV, see Table 3. Therefore, following papers [70,94,95], the temperature dependences of the electrical resistance $\rho(T)$ and thermoEMF $S(T)$ in the whole temperature range 6–300 K can be described on the basis of the band energy scheme shown in Fig. 9 of our previous work [70] for Fe-doped ZnO-based ceramics. This scheme has fully explained the changes of carrier transport mechanisms observed in our experiments for both the undoped and doped samples.

5. Resistivity, Hall effect and thermoelectric properties at room temperature

Let us compare the room temperature values of Seebeck coefficient S_{300} and resistivity ρ_{300} with concentration of electrons n

estimated from Hall constant R_H in the studied ZnO-based ceramics. These data together with the calculated values of the power factor $P = S^2/\rho$ are presented in Table 4 and in Figs. 17 and 18.

The joint analysis of the parameters, presented in Table 4 and Figs. 17 and 18, allows to establish certain correlations between S_{300}, ρ_{300}, n_{300} and P_{300} values when doping of ZnO ceramics.

First correlation consists in the fact that for the overwhelming number of the studied ceramic samples, doping with iron and cobalt leads to an increase of ρ_{300} as compared to the undoped zinc oxide ceramic samples. In so doing, as follows from Fig. 17a, the resistivity ρ_{300} tends to fall monotonically with increasing electron concentration n_{300} as a result of doping, regardless of the type of dopant.

Second correlation, following from Table 4, shows that doping with Co gives small increase of S_{300} values (as a rule, in 1.3–1.6 times) as compare with the undoped Sample 2 (as was noted in paragraph 2, we used two different ZnO powders for preparation of Fe- and Co-doped ceramics which have different values of S_{300} in Table 4). At the same time, Fe doping results in more strong growth of S_{300} as compared to the undoped sample 1, approaching the values up to 955 ± 55 μV/K for the sample 11 (as was noted in paragraph 2, we used two different ZnO powders for preparation of Fe- and Co-doped ceramics which have different values of S_{300} in Table 4).

As is seen from Fig. 17c, there are two fundamentally different trends in $S(\rho)$ dependences for the studied ceramics $(ZnO)_z[(Fe_xO_y)]_{1-z}$ and $(ZnO)_z[CoO]_{1-z}$. Black and blue dots, falling into the oval in Fig. 17c and refering to the undoped ZnO and $(ZnO)_z[CoO]_{1-z}$ ceramics, show that ρ_{300} practically does not affect the value of S_{300}. At the same time, the $S(\rho)$ dependence for $(ZnO)_z[Fe_xO_y]_{1-z}$ ceramics (red dots) looks like $S(n)$ in Fig. 18b. Note that we could not observe the same behavior $S(n)$ for Co-doped samples because they were characterized by strong LSPR due to high disordering, that did not allow to make measurements of Hall effect.
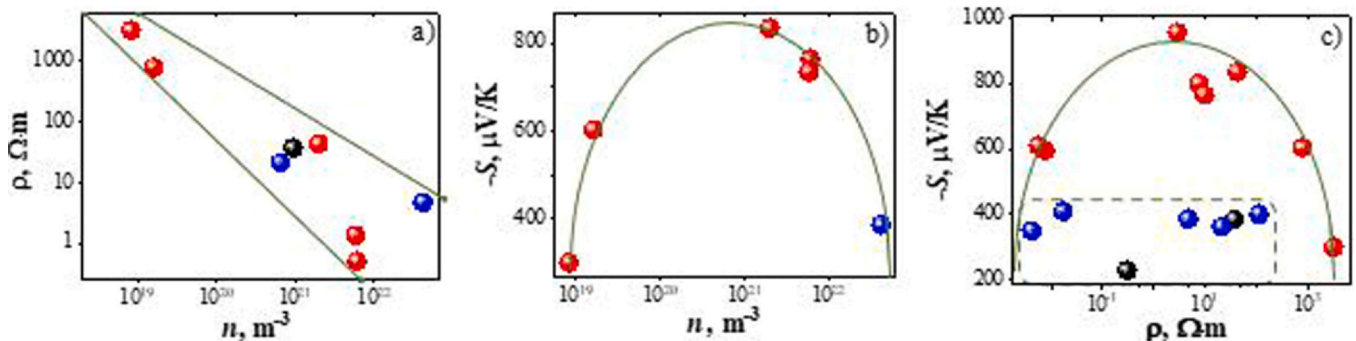

Fig. 17. Dependences of resistivity (*a*) and Seebeck coefficient (*b*) on electron concentration n as well as Seebeck coefficient on resistivity (*c*) for the studied ZnO-based ceramics. The area in Fig. (*c*), limited by an oval, refers to samples of undoped zinc oxide and ceramics doped with cobalt.
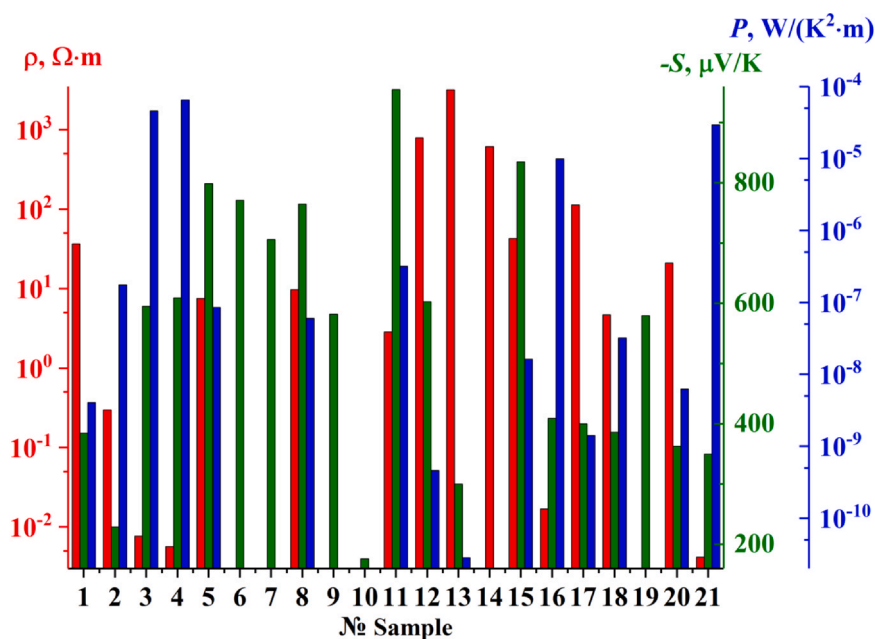
Fig. 18. Distribution of resistivity (red bars), Seebeck coefficient (green bars) and power factor (blue bars) by the studied samples of ceramics.

The described character of $S(n)$ and $\rho(n)$ dependences in the studied Fe-doped ceramics is in good agreement with the known models describing thermoelectric properties in doped semiconductors (see, for example [96,97]) and show that maximal S_{300} are observed only for any optimized values of concentration of carriers and resistivity.

The observed strong increase of Seebeck coefficient S_{300} due to doping with iron as well as similarity of $S(n)$ and $\rho(n)$ dependences in the studied Fe-doped ceramics indicates allows to ascribe such difference to their different phase states: the $(ZnO)_z[CoO]_{1-z}$ samples are single-phase solid solutions with a wurtzite lattice (the lack of $ZnCo_2O_4$), while the samples $(ZnO)_z[(Fe_xO_y)]_{1-z}$ are two-phase, since they have particles of zinc ferrite $ZnFe_2O_4$ embedded into in the wurtzite matrix. This means that an increase in the Seebeck coefficient from about (230−400) $\mu V/K$ for the undoped ZnO up to about 1000 $\mu V/K$ at the optimized electron concentration after doping with iron is just due to the presence of secondary ferritic phase $ZnFe_2O_4$. This is also in agreement with paper [24]. Moreover, this is supported additionally, in our opinion, by the fact that for more inhomogeneous samples $(ZnO)_z[(Fe_xO_y)]_{1-z}$ obtained by one-stage synthesis (according to EDX, XRD, MS and RS, they contained more concentration of ferritic phase), on average, have higher values of the Seebeck coefficient than ceramics obtained by the two-stage technology (see, Table 4).

Calculations of the power factor $P = (S^2/\rho)$ for the studied samples, presented in Table 4 and in Fig. 18, evidence that its highest values (of the order of 10^{-5} W/K·m) are achieved for ceramics with the lowest values of resistivity. These include the most heterogeneous ceramics $(ZnO)_z(CoO)_{1-z}$ (samples 16 and 21) and $(ZnO)_z(Fe_xO_y)_{1-z}$ (samples 3 and 4), obtained by the one-stage technologies.

6. Conclusions

We have shown the influence of the structure (phase and chemical composition, grain sizes, magnetic status, porosity), type of doping agents and temperature on the electrical (resistivity, Hall effect, Seebeck coefficient) and magnetic (magnetization, Messbauer spectra) properties of ceramic compositions $(ZnO)_z[(TM)_xO_y]_{1-z}$, where transition metals TM = Fe and Co with $0 \le x \le 3$, $1 \le y \le 4$, $0.5 \le z \le 10$ wt%). Samples were prepared by one-step and/or

two-step technologies using oxides Fe_xO_y or CoO as doping agents. EDX, XRD, RS, MS and magnetization have showed that phase composition of ceramic samples was dependent on type of dopant. In $(ZnO)_z(Fe_xO_y)_{1-z}$ samples three phases were observed, as a rule: wurtzite $Zn_{1-\delta}Fe_\delta O$, ferrite $ZnFe_2O_4$ with a spinel structure, as well as residual cubic iron oxides. In $(ZnO)_z(CoO)_{1-z}$ samples only solid solutions with wirtzite structure were observed at $z \le 10$ wt%. Using SEM method, it was found that the sizes of the most grains with wurtzite structure decrease from several tens of micrometers, when using one-step synthesis, to the submicron level for the case of two-step technology. It was proved that compaction and two-stage (presintering and post-sintering) annealing of powder mixtures $(ZnO)_{90}(\alpha-Fe_2O_3)_{10}$ in air results in the formation of ceramics with paramagnetic properties at room temperature due to the presence of $ZnFe_2O_4$ ferrite with spinel structure. At $T \le 10$ K, $ZnFe_2O_4$ is characterized with the increased coercive force (350–450 Oe), which is due to its transition to antiferromagnetic state. The use of Fe_3O_4 as a doping agent leads to the formation of ceramics, which possess weak ferromagnetic properties at room temperature due to the presence of residual $\alpha-Fe_2O_3$ phase, which contributes to the increase in magnetic susceptibility and coercive force (up to 300 Oe) at room temperature.

It was found that the incorporation of iron into the wurtzite $Zn_{1-\delta}Fe_\delta O$ phase, in addition to shallow donors due to native defects with an ionization energy of about 0.04–0.05 eV, deep donor centers with an ionization energy of about 0.24–0.37 eV were formed. Temperature dependences of electrical resistivity $\rho(T)$ in the temperature range of 6–300 K in the undoped and Co-doped ZnO-based ceramics were characterized by a variable energy of activation, which indicates strong disordering and inhomogeneity of the samples structure resulting in the formation of a large-scale potential relief. As a result, in the undoped ZnO and solid solutions ZnO < TM > we observe sequentially 4 mechanisms of carrier transport with temperature increase – from the VRH conductivity with Mott (lower than 15 K) and Shklovsky-Efros (in the region $20 < T < 40$ K) mechanisms to the percolative carrier transport at $50 < T < 150$ K, and then to standard conduction by C-band above 150–200 K. The doping of ZnO have shown very strong influence of the dopant type on Seebeck coefficient S. When doping with iron, the Seebeck coefficient S at 300 K is increased in average. In so doing,

the S_{300} value itself depends on electron concentration n of the $(ZnO)_z(Fe_xO_y)_{1-z}$ samples going through the maximum about 1000 μV/K at $n = 10^{21}$ m^{-3}. At the same time, ZnO doping with Co only slightly increase the S_{300} values. We attributed this growth of S_{300} values with Fe doping to the formation of secondary ferritic phase $ZnFe_2O_4$ embedded into wurtzite matrix. Calculations of the power factor $P = (S^2/\rho)$ for the studied samples evidenced their highest values (of the order of 10^{-5} W/K·m) in ceramics with the lowest resistivity values for the case of both dopants.

CRediT authorship contribution statement

Declaration of Competing Interest

The authors declare that they have no known competing financial interests or personal relationships that could have appeared to influence the work reported in this paper.

Acknowledgments

References

[1] S.D. Ponja, S. Sathasivam, I.P. Parkin, C.J. Carmalt, Highly conductive and transparent gallium doped zinc oxide thin films via chemical vapor deposition, Sci. Rep. 10 (2020) 638, https://doi.org/10.1038/s41598-020-57532-7

[2] Y.-P. Lee, Ch-Ch Lin, Ch-Ch Hsiao, P.-A. Chou, Y.-Y. Cheng, Ch-Ch Hsieh, Ch-A. Dai, Nanopiezoelectric devices for energy generation based on ZnO nanorods/flexible-conjugated copolymer hybrids using all wet-coating processes, Micromachines 11 (1) (2020) 14, https://doi.org/10.3390/mi11010014

[3] L.M. Levinson, Shin-ichi Hirano (Eds.), Ceramic Transactions, Grain Boundaries and Interfacial Phenomena in Electronic Ceramics, 41 American Ceramic Society, Westerville, 0-944904-73-4, 1994.

[4] A. Sawalha, M. Abu-Abdeen, A. Sedky, Electrical conductivity study in pure and doped ZnO ceramic system, Physica B 404 (2009) 1316–1320, https://doi.org/10.1016/j.physb.2008.12.017

[5] D. Winarski, Synthesis and characterization of transparent conductive zinc oxide thin films by sol-gel spin coating method, Graduate College of Bowling Green State University: Thesis of master science, 2015. ⟨http://rave.ohiolink.edu/etdc/view?acc_num=bgsu1434124579⟩.

[6] H. Chen, L. Zheng, J. Zeng, G. Li, Effect of Sr doping on nonlinear current–voltage properties of ZnO-based ceramics, J. Electron. Mater. 50 (2021) 4096–4103, https://doi.org/10.1007/s11664-021-08960-2

[7] J. Li, S. Yang, Y. Pu, D. Zhu, Effects of pre-calcination and sintering temperature on the microstructure and electrical properties of ZnO-based varistor ceramics, Mater. Sci. Semicond. Process. 123 (2021) 105529, https://doi.org/10.1016/j.mssp.2020.105529

[8] M.A. Mohammed, S. Izman, M.N. Alias, S. Rajoo, M.B. Uday, N.H. Obayes, M.F. Omar, A review of thermoelectric ZnO nanostructured ceramics for energy recovery, Int. J. Eng. Technol. 7 (2.29) (2018) 27–30.

[9] H. Colder, E. Guilmeau, C. Harnois, S. Marinel, R. Retoux, E. Savary, Preparation of Ni-doped ZnO ceramics for thermoelectric applications, J. Eur. Ceram. Soc. 31 (15) (2011) 2957–2963, https://doi.org/10.1016/j.jeurceramsoc.2011.07.006

[10] A. Jeong, K. Suekuni, M. Ohtakia, B.-K. Jang, Thermoelectric properties of In- and Ga-doped spark plasma sintered ZnO ceramics, Ceram. Int. 47 (17) (2021) 23927–23934, https://doi.org/10.1016/j.ceramint.2021.05.101

[11] X. Liang, Thermoelectric transport properties of naturally nanostructured Ga–ZnO ceramics: effect of point defect and interfaces, J. Eur. Ceram. Soc. 36 (7) (2016) 1643–1650, https://doi.org/10.1016/j.jeurcerasoc.2016.02.017

[12] X. Liang, Thermoelectric transport properties of Fe-enriched ZnO with high-temperature nanostructure refinement, ACS Appl. Mater. Interfaces 7 (15) (2015) 7927–7937, https://doi.org/10.1021/am509050a

[13] S. Walia, S. Balendhran, H. Nili, S. Zhuiykov, G. Rosengarten, Q.H. Wang, M. Bhaskaran, S. Sriram, M.S. Strano, K. Kalantar-zadeh, Transition metal oxides – thermoelectric properties, Prog. Mater. Sci. 58 (8) (2013) 1443–1489, https://doi.org/10.1016/j.pmatsci.2013.06.003

[14] P. Li, H. Zhang, C. Gao, G. Jiang, Z. Li, Electrical property of Al/La/Cu modified ZnO-based negative temperature coefficient (NTC) ceramics with high ageing stability, J. Mater. Sci.: Mater. Electron. 30 (2019) 19598–19608, https://doi.org/10.1007/s10854-019-02333-6

[15] A. Quarta, R.M. Novais, S. Bettini, M. Iafisco, R.C. Pullar, C. Piccirilloa, A sustainable multi-function biomorphic material for pollution remediation or UV absorption: aerosol assisted preparation of highly porous ZnO-based materials from cork templates, J. Environ. Chem. Eng. 7 (2019) 102936, https://doi.org/10.1016/j.jece.2019.102936

[16] Q. Sun, G. Li, T. Tian, J. Zeng, K. Zhao, L. Zheng, M. Barre, J. Dittmer, F. Gouttenoire, A. Rousseau, A.H. Kassiba, Co-doping effects of (Al, Ti, Mg) on the microstructure and electrical behavior of ZnO-based ceramics, J. Am. Ceram. Soc. 103 (2020) 3194–3204, https://doi.org/10.1111/jace.16999

[17] D.V. Vu, D.H. Le, C.X. Nguyen, T.Q. Trinh, Comparison of structural and electric properties of ZnO-based n-type thin films with different dopants for thermoelectric applications, J. Sol. -Gel Sci. Technol. 91 (2019) 146–153, https://doi.org/10.1007/s10971-019-05024-0

[18] M.A. White, S.T. Ochsenbein, D.R. Gamelin, Colloidal nanocrystals of wurtzite Zn$_{1-x}$Co$_x$O (0 < x < 1): models of spinodal decomposition in an oxide diluted magnetic semiconductor, Chem. Mater. 20 (2008) 7107–7116, https://doi.org/10.1021/cm802280g

[19] C. Li, Y. Bando, M. Nakamura, N. Kimizuka, Antiphase modulated structure of Fe2O3(ZnO)15 studied by high-resolution electron microscopy, J. Solid State Chem. 142 (1999) 174–179 https://doi.org/jssc.1998.802.

[20] O. Koster-Scherger, H. Schmid, N. Vanderschaeghe, F. Wolf, W. Mader, ZnO with additions of Fe$_2$O$_3$: microstructure, defects, and Fe solubility, J. Am. Ceram. Soc. 90 (2007) 3984–3991, https://doi.org/10.1111/j.1551-2916.2007.02066.x

[21] X. Li, Z. Yu, X. Long, P. Lin, X. Cheng, Y. Liu, C. Cao, H. Zhang, G. Wu, R. Yu, Synthesis and magnetic properties of Al doped Zn$_{0.995}$MN$_{0.005}$O powers, Appl. Phys. Lett. 94 (2009) 252501, https://doi.org/10.1063/1.3159469

[22] K. Park, J.K. Seong, G.H. Kim, NiO Added Zn$_{1-x}$Ni$_x$O (0 < x < 0.05) for thermoelectric power generation, J. Alloy. Compd. 473 (2009) 423–427, https://doi.org/10.1016/j.jallcom.2008.05.101

[23] A. Virdiana, S. Muhammadya, M.A. Naradipa, R. Widita, A. Rusydi, Y. Darma, Enhancing photon absorption and conductivity of ZnO film by Fe doping: experimental and first-principle perspectives, Ceram. Int. 46 (17) (2020) 27110–27118, https://doi.org/10.1016/j.ceramint.2020.07.188

[24] X. Liang, Thermoelectric transport properties of Fe-enriched ZnO with high-temperature nanostructure refinement, ACS Appl. Mater. Interfaces 7 (15) (2015) 7927–7937, https://doi.org/10.1021/am509050a

[25] M. Ohtaki, T. Tsubota, K. Eguchi, H. Arai, High-temperature thermoelectric properties of (Zn$_{1-x}$Al$_x$)O, J. Appl. Phys. 79 (1996) 1816, https://doi.org/10.1063/1.360976

[26] T. Tsubota, M. Ohtaki, K. Eguchi, H. Arai, Thermoelectric properties of Al-doped ZnO as a promising oxide material for high- temperature thermoelectric conversion, J. Mater. Chem. 7 (1997) 85–90, https://doi.org/10.1039/A602506D

[27] Y. Fujishiro, M. Miyata, M. Awano, K. Maeda, Effect of microstructural control on thermoelectric properties of hot-pressed aluminum-doped zinc oxide, J. Am. Ceram. Soc. 86 (2003) 2063–2066, https://doi.org/10.1111/j.1151-2916.2003.tb03610.x

[28] K. Park, J.W. Choi, S.J. Kim, G.H. Kim, Y.S. Cho, Zn$_{1-x}$Bi$_x$O (0 < x < 0.02) for Thermoelectric Power Generations, J. Alloy. Compd. 485 (2009) 532–537, https://doi.org/10.1016/j.jallcom.2009.06.021

[29] M.A. White, S.T. Ochsenbein, D.R. Gamelin, Colloidal nanocrystals of wurtzite Zn$_{1-x}$Co$_x$O (0 < x < 1): models of spinodal decomposition in an oxide diluted magnetic semiconductor, Chem. Mater. 20 (2008) 7107–7116, https://doi.org/10.1021/cm802280g

[30] X. Li, Z. Yu, X. Long, P. Lin, X. Cheng, Y. Liu, C. Cao, H. Zhang, G. Wu, R. Yu, Synthesis and magnetic properties of Al doped Zn$_{0.995}$Mn$_{0.005}$O powers, Appl. Phys. Lett. 94 (2009) 252501, https://doi.org/10.1063/1.3159469

[31] K. Park, J.K. Seong, G.H. Kim, NiO Added Zn$_{1-x}$Ni$_x$O (0 < x < 0.05) for THermoelectric Power Generation, J. Alloy. Compd. 473 (2009) 423–427, https://doi.org/10.1016/j.jallcom.2008.05.101

[32] H. Colder, E. Guilmeau, C. Harnois, S. Marinel, R. Retoux, E. Savary, Preparation of Ni-doped ZnO ceramics for thermoelectric applications, J. Eur. Ceram. Soc. 31 (2011) 2957–2963, https://doi.org/10.1016/j.jeurceramsoc.2011.07.006

[33] K. Park, J.K. Seong, S. Nahm, Improvement of thermoelectric properties with the addition of Sb to ZnO, J. Alloy. Compd. 455 (2008) 331–335, https://doi.org/10.1016/j.jallcom.2007.01.080

[34] K. Park, J.K. Seong, Y. Kwon, S. Nahm, W.-S. Cho, Influence of SnO$_2$ addition on the thermoelectric properties of Zn$_{1-x}$Sn$_x$O (0.01 ≤ x ≤ 0.05), Mater. Res. Bull. 43 (2008) 54–61, https://doi.org/10.1016/j.materresbull.2007.02.018

[35] H. Yamaguchi, Y. Chonan, M. Oda, T. Komiyama, T. Aoyama, S. Sugiyama, Thermoelectric properties of ZnO ceramics Co-doped with Al and transition metals, J. Electron. Mater. 40 (5) (2011) 723–727, https://doi.org/10.1007/s11664-011-1529-9

[36] Z.-H. Wu, H.-Q. Xie, Y.-B. Zhai, Preparation and thermoelectric properties of Co-doped ZnO synthesized by sol-gel, J. Nanosci. Nanotechnol. 15 (4) (2015) 3147–3150, https://doi.org/10.1166/jnn.2015.9658

[37] B. Zhu, C. Chen, Z.C. Yao, J.Y. Chen, C. Jia, Z.H. Wang, R.M. Tian, L. Tao, F. Xue, H.H. Hong, Multiple doped ZnO with enhanced thermoelectric properties, J. Eur. Ceram. Soc. 41 (7) (2021) 4182–4188, https://doi.org/10.1016/j.jeurceramsoc.2021.01.054

[38] P. Pascariua, M. Homocianu, ZnO-based ceramic nanofibers: preparation, properties and applications, Ceram. Int. 45 (9) (2019) 11158–11173, https://doi.org/10.1016/j.ceramint.2019.03.113

[39] H.N. Sahu, B.N. Sherikar, Synthesis of Fe doped ZnO spintronic nano powders by solution combustion method & their characterization, Int. J. Eng. Res. Technol. 6 (2017) 591–596.

[40] D. Chiba, N. Shibata, A. Tsukazaki, Co thin films deposited directly on ZnO polar surfaces, Nature 6 (2016) 1–9, https://doi.org/10.1038/srep38005

[41] M. Mustaqima, C. Liu, ZnO-based nanostructures for diluted magnetic semiconductor, Turk. J. Phys. 38 (2014) 429–441, https://doi.org/10.3906/fiz-1405-17

[42] S.J. Pearton, D.P. Norton, Y.W. Heo, L.C. Tien, M.P. Ivill, Y. Li, B.S. Kang, F. Ren, J. Kelly, A.F. Hebard, ZnO spintronics and nanowire devices, J. Electron. Mater. 35 (2006) 862–868 https://doi.org/10.1007/BF02692541.

[43] A. Roychowdhury, A.K. Mishra, S.P. Pati, D. Das, Synthesis and characterization of multifunctional Fe3O4-ZnO nanocomposite, AIP Conf. Proc. 1447 (2012) 283–284, https://doi.org/10.1063/1.4709990

[44] R. Master, R.J. Choudhary, D.M. Phase, Structural and magnetic properties of epitaxial Fe3O4 / ZnO and ZnO / Fe3O4 bilayers grown on c-Al 2 O 3 substrate, J. Appl. Phys. 108 (2010) 103, https://doi.org/10.1063/1.3483957 909-1-5.

[45] P. Zou, X. Hong, X. Chu, Y. Li, Y. Liu, Multifunctional Fe3O4/ZnO nanocomposites with magnetic and optical properties, J. Nanosci. Nanotechnol. 10 (2010) 1992–1997, https://doi.org/10.1166/jnn.2010.2098

[46] A. Hasanpur, M. Niyaifar, M. Asan, J. Amighian, Synthesis and characterization of Fe3O4 and ZnO nanocomposites by the sol–gel method, J. Magn. Magn. Mater. 334 (2013) 41–44, https://doi.org/10.1016/j.jmmm.2013.01.016

[47] H.L. Liu, J.H. Wu, J.H. Min, X.Y. Zhang, Y.K. Kim, Tunable synthesis and multi-functionalities of Fe3O4–ZnO hybrid core-shell nanocrystals, Mater. Res. Bull. 48 (2013) 551–558, https://doi.org/10.1016/j.materresbull.2012.11.051

[48] M. Machovsky, I. Kuritka, Z. Kozakova, Microwave assisted synthesis of nanostructured Fe3O4/ZnO microparticles, Mater. Lett. 86 (2012) 136–138, https://doi.org/10.1016/j.matlet.2012.07.038

[49] J. Xia, A. Wang, X. Liu, Z. Su, Preparation and characterization of bifunctional, Fe3O4/ZnO nanocomposites and their use as photocatalysts, Appl. Surf. Sci. 257 (2011) 9724–9732, https://doi.org/10.1016/j.apsusc.2011.05.114

[50] A. Kostopoulou, F. T˘etiot, I. Tsiaoussis, M. Androulidaki, P.D. Cozzoli, A. Lappas, Colloidal anisotropic ZnO–Fe@FexOy nanoarchitectures with fluorescence interface-mediated exchange-bias and band-edge ultraviolet fluorescence, Chem. Mater. 24 (2012) 2722–2732, https://doi.org/10.1021/cm3008182

[51] J. Cao, W. Fu, H. Yang, Q. Yu, Y. Zhang, S. Wang, H. Zhao, Y. Sui, X. Zhou, W. Zhao, Y. Leng, H. Zhao, H. Chen, X. Qi, Fabrication, characterization and application in electromagnetic wave absorption of flower-like ZnO/Fe3O4 nanocomposites, Mater. Sci. Eng. B 175 (2010) 56–59, https://doi.org/10.1016/j.mseb.2010.06.020

[52] J. Wan, H. Li, K. Chen, Synthesis and characterization of Fe3O4@ZnO core–shell structured nanoparticles, Mater. Chem. Phys. 114 (2009) 30–32, https://doi.org/10.1016/j.matchemphys.2008.10.039

[53] P. Li, B.L. Guo, H.L. Bai, Spin injection from epitaxial Fe 3 O 4 films to ZnO films, J. Appl. Phys. 109 (2011) 013908, https://doi.org/10.1063/1.3528202 -1-3.

[54] Z. Wang, L. Wu, J. Zhou, B. Shen, Z. Jiang, Enhanced microwave absorption of Fe3O4 nanocrystals after heterogeneously growing with ZnO nanoshell, RSC Adv. 3 (2013) 3309–3315, https://doi.org/10.1039/c2ra23404a

[55] N.-H. Cho, T.-C. Cheong, J.H. Min, J.H. Wu, S.J. Lee, D. Kim, J.-S. Yang, S. Kim, Y.K. Kim, S.-Y. Seong, A multifunctional core–shell nanoparticle for dendritic cell-based cancer immunotherapy, Nat. Nanotechnol. 6 (2011) 675–682, https://doi.org/10.1038/nnano.2011.149

[56] S. Singh, K.C. Barick, D. Bahadur, Fe3O4 embedded ZnO nanocomposites for the removal of toxic metal ions, organic dyes and bacterial pathogens†, J. Mater. Chem. A 1 (2013) 3325–3333, https://doi.org/10.1039/c2ta01045c

[57] S. Karpova, V.A. Moshnikov, S.V. Mjakin, E.S. Kolovangin, Surface functional composition and sensor properties of ZnO, Fe2O3, and ZnFe2O4, Semiconductors 47 (2013) 369–372, https://doi.org/10.1134/S1063782613030123

[58] A. Parra-Palomino, R. Singhal, O. Perales Perez, S. Dussan-Devia, M.S. Tomar, Low-temperature chemical solution synthesis and characterization of nano-crystalline Fe-doped ZnO, Nano Sci. Technol. Inst. -Nanotech 2007 (4) (2007) 297–300.

[59] I. Kazeminezhad, S. Saadatmand, R. Yousefi, Effect of transition metal elements on the structural and optical properties of ZnO nanoparticles, Bull. Mater. Sci.: Indian Acad. Sci. 39 (2016) 719–724, https://doi.org/10.1007/s12034-016-1206-y

[60] A. Jagannatha Reddy, M.K. Kokila, H. Nagabhushana, S.C. Sharma, J.L. Rao, C. Shivakumara, B.M. Nagabhushana, R.P.S. Chakradhar, Structural, EPR, photo and thermoluminescence properties of ZnO:Fe nanoparticles, Mater. Chem. Phys. 133 (2012) 876–883, https://doi.org/10.1016/j.matchemphys.2012.01.111

[61] M. Silambarasan, S. Saravanan, T. Soga, Raman and photoluminescence studies of Ag and Fe-doped ZnO, Int. J. ChemTech Res. 7 (2015) 1644–1650.

[62] A. Janotti, C.G. Van de Walle, Fundamentals of zinc oxide as a semiconductor, Rep. Prog. Phys. 72 (2009) 26501, https://doi.org/10.1088/0034-4885/72/12/126501 -1-29.

[63] A. Janotti, C.G. Van de Walle, Native point defects in ZnO, Phys. Rev. B 76 (2007) 165202, https://doi.org/10.1103/PhysRevB.76.165202 -1-22.

[64] X.L. Wu, G.G. Siu, C.L. Fu, H.C. Ong, Photoluminescence and cathodoluminescence studies of stoichiometric and oxygen-deficient ZnO films, Appl. Phys. Lett. 78 (2001) 2285–2287, https://doi.org/10.1063/1.1361288

[65] L. Schmidt-Mende, J.L. MacManus-Driscoll, ZnO – nanostructures, defects, and devices, Mater. Today 10 (2007) 40–48, https://doi.org/10.1016/S1369-7021(07)70078-0

[66] S.-P. Chiu, Y.-H. Lin, J.-J. Lin, Electrical conduction mechanisms in natively doped ZnO nanowires, Nanotechnology 20 (2009) 1–8, https://doi.org/10.1088/0957-4484/20/1/015203

[67] J. Rodriguez-Carvajal, Recent advances in magnetic structure determination by neutron powder diffraction, Physica B 192 (1993) 55–69, https://doi.org/10.1016/0921-4526(93)90108-I

[68] D.G. Rancourt, Accurate site population form Mössbauer spectroscopy, Nucl. Instrum. Method B 44 (1989) 199–210, https://doi.org/10.1016/0168-583X(89)90428-X

[69] A.S. Fedotov, A.V. Pashkevich, L.A. Bliznyuk, J. Kasiuk, A.K. Fedotov, N.A. Basov, I.A. Svito, M. Budzyński, M. Wierteł, /8P. Żukowski, Electric properties of composite ZnO-based ceramics doped with Fe, Prz. Elektrotech. 94 (2018) 197–199, https://doi.org/10.15199/48.2018.03.39

[70] A.V. Pashkevich, A.K. Fedotov, Yu.V. Kasyuk, L.A. Bliznyuk, J.A. Fedotova, N.A. Basov, A.S. Fedotov, I.A. Svito, E.N. Poddenezhny, Structure and electric properties of zink oxide−based ceramics doped with iron, Mater. Electron. Eng. 21 (2018) 133–145, https://doi.org/10.17073/1609-3577-2018-3-133-145

[71] A.R. Vazquez-Olmos, M. Abatal, R.Y. Sato-Berru, G.K. Pedraza-Basulto, V. Garcia-Vazquez, A. Sainz-Vidal, R. Perez-Bañuelos, A. Quiroz, Mechanosynthesis of MFe2O4 (M = Co, Ni, and Zn) magnetic nanoparticles for Pb removal from aqueous solution, J. Nanomater. (2016) 1–9, https://doi.org/10.1155/2016/9182024

[72] L.I. Granone, A.C. Ulpe, L. Robben, S. Klimke, M. Jahns, F. Renz, T.M. Gesing, T. Bredow, R. Dillert, D.W. Bahnemann, Effect of the degree of inversion on optical properties of spinel ZnFe2O4, Phys. Chem. Chem. Phys. 20 (2018) 28267–28278, https://doi.org/10.1039/c8cp05061a

[73] N. Romcevic, R. Kostic, M. Romcevic, B. Hadzic, I. Kuryliszyn-Kudelska, W. Dobrowolski, U. Narkiewicz, D. Sibera, Raman scattering from ZnO(Fe) nanoparticles, Acta Phys. Pol. A 114 (2008) 1323–1328, https://doi.org/10.12693/APhysPolA.114.1323

[74] M. Shumm, ZnO-based semiconductors studied Raman spectroscopy: semi-magnetic alloying, doping, and nanostructures, Würzburg: Thesis of PhD, 2008.

[75] Z.W. Wang, P. Lazor, S.K. Saxena, G. Artioli, High-pressure raman spectroscopic study of spinel (ZnCr2O4), J. Solid State Chem. 165 (2002) 165–170, https://doi.org/10.1006/jssc.2002.9527

[76] M. Maletin, E.G. Moshopoulou, A.G. Kontos, E. Devlin, A. Dlimitis, V.T. Zaspalis, L. Nalbandian, V.V. Srdić, Synthesis and structuralcharacterization of In doped ZnFe2O4 nanoparticles, J. Eur. Ceram. Soc. 27 (2007) 4391–4394, https://doi.org/10.1016/j.jeurceramsoc.2007.02.165

[77] A. Milutinović, Z. Lazarević, Č. Jovalekić, I. Kuryliszyn-Kudelska, M. Romčević, S. Kostic, N. Romčević, The cation inversion and magnetization in nanopowder zinc ferrite obtained by soft mechanochemical processing, Mater. Res. Bull. 48 (2013) 4759–4768, https://doi.org/10.1016/j.materresbull.2013.08.020

[78] O.N. Shebanova, P. Lazor, Raman study of magnetite (Fe3O4): laser-induced thermal effects and oxidation, J. Raman Spectrosc. 34 (2003) 845–852, https://doi.org/10.1002/jrs.1056

[79] B.B. Straumal, S.G. Protasova, A.A. Mazilkin, E. Goering, G. Schütz, P.B. Straumal, B. Baretzky, Ferromagnetic behaviour of ZnO: the role of grain boundaries, Beilstein J. Nanotechnol. 7 (2016) 1936–1947, https://doi.org/10.3762/bjnano.7.185

[80] S.J. Stewart, S.J.A. Figueroa, M.B. Sturla, R.B. Scorzelli, F. Garcıa, F.G. Requejo, Magnetic ZnFe2O4 nanoferrites studied by X-ray magnetic circular dichroism and Mössbauer spectroscopy, Physica B 389 (2007) 155–158, https://doi.org/10.1016/j.physb.2006.07.045

[81] F. Bodker, S. Morup, Size dependence of the properties of hematite nanoparticles, Europhys. Lett. 52 (2000) 217–223, https://doi.org/10.1209/epl/i2000-00426-2

[82] Shik Ya, Hall effect and electron mobility in inhomogeneous semiconductors, Sov. Phys. - ZhETP 20 (1974) 14–16.

[83] S.R. Kurtz, A.A. Allerman, J.F. Klein, R.M. Sieg, C.H. Seager, E.D. Jones, The role of nitrogen-induced localization and defects in InGaAsN (= 2% N): comparison of InGaAsN grown by molecular beam epitaxy and metal-organic chemical vapor deposition, Mat. Res. Soc. Symp. Proc. 692 (2002) 21–28, https://doi.org/10.1557/PROC-692-H1.7.1

[84] V.A. Kasiyand, D. Nedeogloa, V. Simashkevi, Electron mobility in heavily doped strongly compensated ZnSe crystals, Phys. State Solidi B 136 (1986) 341–347.

[85] D.C. Look, Recent advances in ZnO materials and devices, Mater. Sci. Eng. B 80 (2001) 383–387, https://doi.org/10.1016/S0921-5107(00)00604-8

[86] Y. Jiang, N.C. Giles, L.E. Halliburton, Persistent photoinduced changes in charge states of transition-metal donors in hydrothermally grown ZnO crystals, J. Appl. Phys. 101 (2007) 093706–093708, https://doi.org/10.1063/1.2723872

[87] O.E. Parfenov, F.A. Shklyaruk, On the temperature dependence of the thermo-electric power in disordered semiconductors, Electron. Opt. Prop. Semicond. 41 (2007) 1021.

[88] K. Seeger, An Introduction, Semiconductor Physics, 9th ed., Springer-Verlag,, Berlin, 2004, https://doi.org/10.1007/978-3-662-09855-4

[89] V.I. Shklovski, A.L. Efros, Electronic properties of Doped Semiconductors, Springer-Verlag,, 1984.

[90] A.F. Kohan, G. Ceder, D. Morgan, First-principles study of native point defects in ZnO, Phys. Rev. B 61 (2000) 15019–15027, https://doi.org/10.1103/PhysRevB.61.15019

[91] C.-C. Lien, C.-Y. Wu, Z.-Q. Li, J.-J. Lin, Electrical conduction processes in ZnO in a wide temperature range 20–500 K, J. Appl. Phys. 110 (2011) 063706, https://doi.org/10.1063/1.3638120 -1-7.

[92] V. Quemener, L. Vines, E.V. Monakhov, B.G. Svensson, Iron related donor-like defect in zinc oxide, Appl. Phys. Lett. 102 (2013) 232102, https://doi.org/10.1063/1.4809941 -1-3.

[93] N.F. Mott, E.A. Davis, Electronic Processes in Non-Crystalline Materials, 2nd ed., Clarendon,, Oxford, 1979.

[94] H. von Wenckstern, H. Schmidt, M. Grundmann, M.W. Allen, P. Miller, R.J. Reeves, S.M. Durbin, Defects in hydrothermally grown bulk ZnO, J. Appl. Phys. 91 (2007) 022913, https://doi.org/10.1063/1.2757097 -1-3.

[95] V.D. Kagan, Electron capture by charged impurities in semiconductors under conditions of spatial diffusion, Phys. Solid State 47 (2005) 446–450.

[96] H.J. Goldsmith, Introduction to the Thermoelectricity, Springer-Verlag,, Berlin, Heidelberg, 2010 https://10.1007/978-3-642-00716-3.

[97] D.M. Rowe (Ed.), Handbook of Thermoelectrics, CRC Press, Boca Raton, 1995.